

# **Higgs production at the FCC-ee in the missing energy channel**

**(Higgs-Produktion am FCC-ee im Kanal fehlender Energie)**

von

Janik von Ahnen

geboren am

12.04.1995

Bachelor-Arbeit im Studiengang Physik

Universität Hamburg

2017

1. Gutachter: Dr. Krisztian Peters
2. Gutachter: Prof. Dr. Elisabetta Gallo



# Abstract

The discovery of the Higgs boson in July 2012 by the ATLAS and CMS collaborations opened new doors for the search for physics beyond the Standard Model. In particular, the presence of new particles and interactions might be deduced indirectly via precision measurements.

One way to conduct these precise measurements is with a circular  $e^+e^-$ -collider. The Future Circular Collider (FCC) design study has made a great effort over the past few years in investigating a promising example of such a collider and its discovery potential.

The two most important processes for Higgs production at these colliders are Higgsstrahlung and vector boson fusion. The corresponding cross sections can be measured in the missing energy channel ( $\nu\bar{\nu}(H \rightarrow b\bar{b})$ ).

In this work the effect of detector parameters on the precision with which  $\sigma_{VBF+HZ}(\sigma_{VBF}) \times BR(H \rightarrow b\bar{b})$  at  $\sqrt{s} = 240$  (350) GeV can be measured in this channel is studied. The ILD, a detector specifically designed for a  $e^+e^-$ -collider, is compared to several variations of the CMS detector and shows an increase in precision ranging from 20-100%. The tracker radius, the tracker efficiency and the energy resolution of the hadronic calorimeter are identified as important parameters for a precise measurement. These results can be helpful for the efficient design of a detector at a future  $e^+e^-$ -collider.

## Zusammenfassung

Die Entdeckung des Higgs Bosons im Juli 2012 von der ATLAS und der CMS Kollaboration eröffnet neue Möglichkeiten zur Entdeckung von Physik jenseits des Standard Models. Neue Teilchen und Wechselwirkungen könnten indirekt mit präzisen Messungen entdeckt werden. Eine Möglichkeit für eine präzise Messung bietet ein ringförmiger  $e^+e^-$  Beschleuniger. Die Future Circular Collider (FCC) design study untersucht seit mehreren Jahren das Potential eines solchen Beschleunigers.

Zwei Prozesse zur Erzeugung von Higgs Bosonen, welche an einem  $e^+e^-$  Beschleuniger dominant sind, sind die Higgsstrahlung und die Fusion mittels zweier vektor Bosonen. Die Zugehörigen Wirkungsquerschnitte können im Kanal der fehlenden Energie gemessen werden.

In dieser Arbeit wurde der Einfluss von Detektorparametern auf die Präzision, mit der  $\sigma_{VBF+HZ}(\sigma_{VBF}) \times BR(H \rightarrow b\bar{b})$  bei  $\sqrt{s} = 240$  (350) GeV gemessen werden kann, untersucht. Der ILD, welcher für einen  $e^+e^-$  Beschleuniger entworfen wurde, wird mit dem CMS Detektor verglichen und zeigt eine Verbesserung der Präzision von 20-100%. Der Radius des Spurdetektors, die Effizienz des Spurdetektors und die Energieauflösung des hadronischen Kalorimeters sind als Parameter mit hohem Einfluss auf die Präzision identifiziert worden. Die Ergebnisse dieser Arbeit können hilfreich für die Gestaltung eines Detektors an einem zukünftigen  $e^+e^-$  Beschleunigers sein.

# Contents

<b>1</b>	<b>Introduction</b>	<b>1</b>
<b>2</b>	<b>Fundamentals</b>	<b>3</b>
2.1	The FCC study . . . . .	3
2.2	The Standard Model . . . . .	4
2.3	CMS Detector . . . . .	4
<b>3</b>	<b>Methods</b>	<b>8</b>
3.1	General information on the analysis . . . . .	8
3.1.1	Event generation . . . . .	8
3.1.2	The FCC software . . . . .	9
3.1.3	$b$ -tagging . . . . .	11
3.2	The missing energy channel at 240 GeV . . . . .	12
3.2.1	Event selection . . . . .	12
3.2.2	Scaling . . . . .	14
3.3	The missing energy channel at 350 GeV . . . . .	16
3.3.1	Event selection . . . . .	16
3.3.2	Scaling . . . . .	16
3.4	Statistical analysis . . . . .	17
3.4.1	Poisson smearing . . . . .	20
3.4.2	Gaussian propagation of uncertainty (POU) . . . . .	23
<b>4</b>	<b>Results</b>	<b>24</b>
4.1	Detector comparison . . . . .	24
4.2	Detector parameter impacts . . . . .	28
4.3	Conclusion . . . . .	31

<b>A PYTHIA sample main program</b>	<b>32</b>
<b>B CMS.py</b>	<b>34</b>
<b>C Eidesstattliche Versicherung</b>	<b>43</b>

# List of Figures

1.1	Cross sections for the production of Higgs bosons at $e^+e^-$ -collisions (taken from ref. [1]). . . . .	2
2.1	Summary of all fundamental particles described by the Standard Model (taken from ref. [2]). . . . .	5
2.2	Overview of the Compact Muon Solenoid detector (taken from ref. [3]). . . . .	7
3.1	Cross sections for different processes and different center of mass energies (taken from ref. [4]). . . . .	9
3.2	Overview of the overall dimension [mm] of the ILD (taken from ref. [5]). . . . .	11
3.3	Impact of the $b$ -tagging weights on the statistics of the WW background after the event selection (see section 3.2.1). The di-jet mass is on the x-axis. . . . .	13
3.4	The mass of the reconstructed $b$ -jets before and after scaling for Higgsstrahlung and VBF (after event selection). . . . .	15
3.5	Di-jet mass distribution for $500 \text{ fb}^{-1}$ and 240 GeV after event selection and scaling. . . . .	15
3.6	Missing mass distribution for $500 \text{ fb}^{-1}$ , 350 GeV and the ILD detector after event selection. . . . .	17
3.7	Missing mass distribution at 350 GeV after scaling and event selection for $500 \text{ fb}^{-1}$ and the ILD detector. . . . .	18
3.8	Missing mass distribution at 350 GeV and $500 \text{ fb}^{-1}$ after scaling and event selection for the CMS detector. . . . .	18
3.9	$(m_{\text{miss}}^{\text{rescaled}})^2$ distribution after event selection with the ILD detector for 350 GeV and $500 \text{ fb}^{-1}$ . . . . .	19
3.10	Reduced $\chi^2$ distribution for functions fitted to the histogram resulting from the fit function. . . . .	21
3.11	Signal yield distribution for 240 GeV and $500 \text{ fb}^{-1}$ . . . . .	22

3.12 Behavior of the error on the uncertainty (equation 3.12). . . . .	22
4.1 Precision achieved with the different detector designs. Poisson smearing and the propagation of uncertainty (POU) are used to obtain the precision. The blue and green points are obtained by a simulation with only Higgsstrahlung, VBF and ZZ. . . . .	25
4.2 Core resolution of the signal function for the different detector designs. . . . .	26
4.3 Signal over background for the different detector designs. . . . .	26
4.4 Uncertainty on the background normalization factor for the different detector designs. . . . .	27
4.5 Distribution of $\xi$ for the leading jet of Higgsstrahlung and different detector designs. . . . .	28
4.6 Precision of $\Delta N_{HZ+VBF}/N_{HZ+VBF}$ while changing the tracker radius of the CMS detector. . . . .	30
4.7 Effect of the energy resolution of the hadronic calorimeter on the precision of the $\Delta N_{HZ+VBF}/N_{HZ+VBF}$ measurement. $\Omega$ is the factor by which the relevant terms are changed. Only signal and ZZ background are simulated for this plot. .	31

# List of Tables

3.1	Number of generated events for each process. . . . .	9
3.2	Cross sections for signal and the most important backgrounds for the missing energy channel at 240 GeV and 350 GeV [6][4]. . . . .	10
3.3	Marginal selection efficiencies [%] for the different processes studied at 240 GeV. .	14
3.4	Marginal selection efficiencies [%] for the different processes studied at 350 GeV. .	16
3.5	Fit ranges and the resulting $\chi^2_{reduced}$ for 240 GeV and 350 GeV fits. . . . .	20
4.1	240 GeV, $\Delta N_{VBF+HZ}/N_{VBF+HZ}$ measurement [%] comparison with the CMS note [6] for the Poisson smearing and the propagation of uncertainty (POU) method. . . . .	25
4.2	350 GeV, $\Delta N_{VBF}/N_{VBF}$ measurement [%]. . . . .	27
4.3	Impact of different detector parameters on the width of the signal at 240 GeV. One parameter in the in-situ CMS simulation is changed by the given factor. The width is given by the standard deviation of a gaussian fitted to the signal. The cluster size determines the size of a cluster which is created if a particle gets measured. . . . .	29

# Chapter 1

## Introduction

In July 2012 the discovery of a new boson with a mass of around  $125 \text{ GeV}/c^2$  with CMS [3] and ATLAS [7] at the Large Hadron Collider (LHC) [8] was announced [9][10]. So far all its properties and couplings are in agreement with the theoretical predictions for the Higgs boson predicted within in the Standard Model [11]. To be able to find new physics beyond the Standard Model (BSM) the search has to go in the direction of higher precision and/or higher energies. After its discovery, the Higgs boson can now be used as a tool to find BSM physics by measuring its properties since the BSM particles are predicted to influence the branching ratios and couplings of the Higgs boson.

To perform these measurements with a sufficient precision, new experiments are needed. One possibility to get precise measurements of the Higgs boson is to build an electron-positron collider. The first article concerning the Future Circular Collider (FCC) design study of a  $e^+e^-$ -collider was published in January 2012 and since then a strong case for an electron-positron collider was made.

There are two major possibilities to produce Higgs bosons in  $e^+e^-$ -collisions:

- Higgsstrahlung: The electron and positron produce an off-shell  $Z^0$  which becomes on shell by radiating a Higgs boson.
- Vector boson fusion (VBF): The electron and positron emit a virtual  $W^\pm$  ( $Z^0$ ) boson each. These two vector boson then fuse to form a Higgs boson.

On the right side of figure 1.1 the Feynman diagrams of the two processes are displayed. The figure shows that the Higgsstrahlung process dominates the cross section at 240 GeV while at 350 GeV the cross section for VBF and Higgsstrahlung ( $HZ$ ,  $Z \rightarrow \nu\bar{\nu}$ ) are almost the same. Also, it displays that in this energy regime the VBF via a  $W^+$  and a  $W^-$  is much more likely

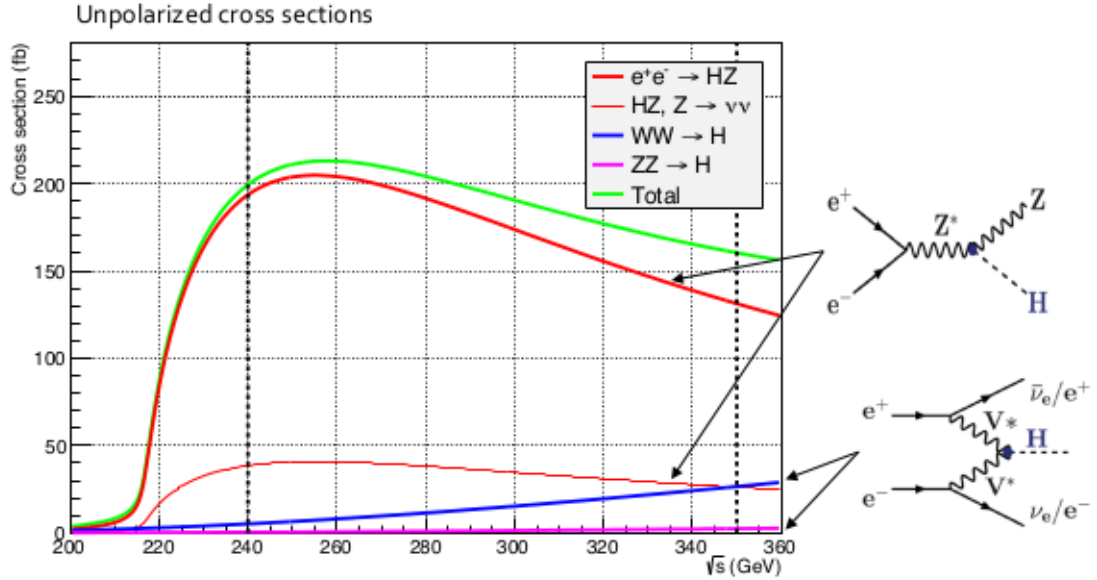


Figure 1.1: Cross sections for the production of Higgs bosons at  $e^+e^-$ -collisions (taken from ref. [1]).

than with two  $Z^0$ . For this reason, the following sections will refer to the fusion of 2  $W^\pm$  with the abbreviation VBF. The missing energy channel  $\nu\bar{\nu}(H \rightarrow b\bar{b})$  is one possibility to measure  $\sigma_{VBF+HZ}(\sigma_{VBF}) \times BR(H \rightarrow b\bar{b})$ .

In this work the effects of detector parameters on the measurement of  $\sigma_{VBF+HZ}(\sigma_{VBF}) \times BR(H \rightarrow b\bar{b})$  at 240 (350) GeV are studied. This is important for an efficient design of the detectors at FCC. To this end, a strategy for the reconstruction and selection of events with the decay of a Higgs boson in the missing energy channel is performed.

For this study, the CMS detector is used as the base. This detector showed a good performance at the LHC and after years of running is a well-understood detector. Therefore, it can be used as a starting point for future experiments which plan to use a general purpose detector.

# Chapter 2

## Fundamentals

### 2.1 The FCC study

The FCC study, hosted by CERN, is an international collaboration of more than 70 institutes [12]. Its goal is to find BSM physics by making high-precision measurements. In some scenarios, the collision energy goes as high as 100 TeV. This study examines mostly the three following types of collisions:

- hadrons (proton-proton and heavy ion)
- electron-positron
- proton-electron

This project is planned to be the successor of LHC. At around the year 2035, the LHC and its High-Luminosity upgrade (HL-LHC) will approach their limits of contributing to the search of BSM physics. At the moment an high luminosity electron-positron ring collider with center of mass energies (cms) of 90 GeV to 400 GeV is a very promising branch of the FCC study. This collider would be located at CERN and have a circumference of 80 to 100 km [1]. At a cms of 90 GeV, the goal is to measure the properties of the gauge bosons of the weak interaction, the  $W^\pm$  and  $Z^0$  bosons. The next interesting collision energy is at 240 GeV. Figure 1.1 shows, that the cross section for Higgs production peaks at  $\sim 260$  GeV, but from 240 GeV to 260 GeV the cross section increases by 6% whereas the power consumption increases by 40% [1]. At 350 GeV the  $t\bar{t}$ -production is kinematically possible, which enables the measurement of top quark properties. In addition, at this energy, the Higgs production cross section consists of a significant part of VBF, which leads to a more precise measurement of this cross section.

## 2.2 The Standard Model

The Standard Model (SM) of particle physics describes all fundamental particles known to date and their interactions<sup>1</sup>. This theory is a quantum field theory and describes the forces between particles via the mediation of gauge bosons. Only three of the four fundamental forces are fully described by the SM. The electromagnetic force is described by the quantum electrodynamic (QED). The QED is a relativistic quantum field theory and describes the force with the mediation of photons. The gauge bosons of the weak interaction are the  $Z^0$  and  $W^\pm$  boson. These two forces are unified within the electroweak interaction. The third force described by the SM is the strong interaction. This force is characterized by the quantum chromodynamics (QCD). The QCD describes the interaction of quarks with the mediation of gluons. The gravitation is the only force not described by the SM and it is one of the biggest problems in modern physics to find a theory that unifies all four fundamental forces.

In figure 2.1 all fundamental particles of the SM are shown. The quarks and leptons are spin- $\frac{1}{2}$  particles whereas gauge bosons have a spin of 1. The Higgs boson has a spin of 0 and is a scalar boson. The coupling of the Higgs to other particles is proportional to their mass. It is important to explain the symmetry breaking and therefore the masses of the gauge bosons. The masses of fermions arise from the Yukawa couplings.

The cross section of a process is directly linked to the number of events, with a certain amount of luminosity, by the following formula:

$$\sigma = \frac{N}{\mathcal{L}_{int}} \quad (2.1)$$

$\sigma$  denotes the cross section,  $N$  the number of events and  $\mathcal{L}_{int}$  the integrated luminosity.

Although the SM is able to describe almost all phenomena with a high accuracy, the SM can not be the last answer as there are things like dark matter, dark energy and gravity which are not yet described by it.

## 2.3 CMS Detector

The Compact Muon Solenoid (CMS) detector is one of the four big experiments at the LHC. This section will give an overview of the CMS detector, that is described in detail in [3].

It is a general purpose detector for pp and PbPb collisions. It was designed to fulfill the follow-

---

<sup>1</sup>This section is based on [13]

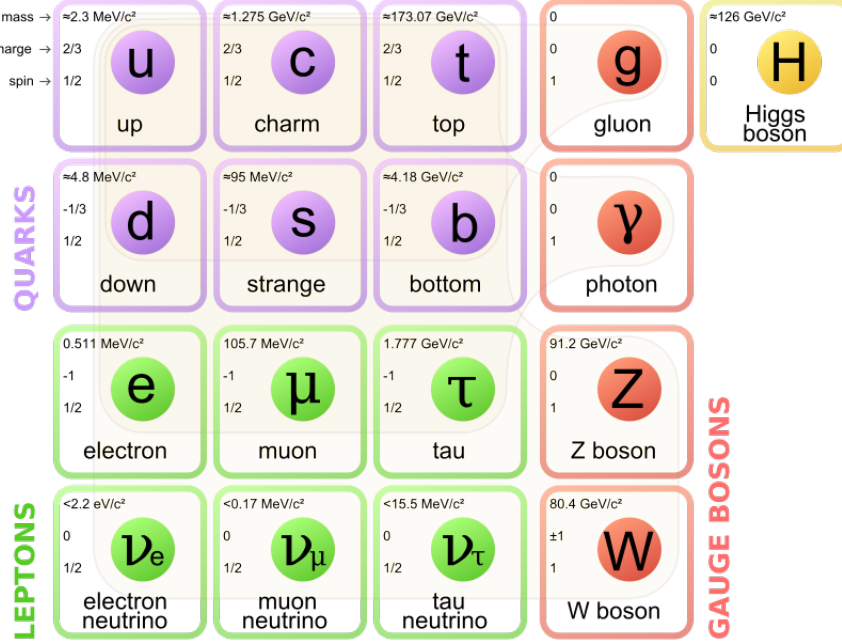


Figure 2.1: Summary of all fundamental particles described by the Standard Model (taken from ref. [2]).

ing requirements:

- Good muon reconstruction. High identification rate and good momentum resolution.
- Good momentum resolution of charged particles and a high efficiency for the inner tracking system.
- Good electromagnetic energy resolution with a wide coverage which leads to efficient photon and lepton isolation.
- Good missing energy resolution. This needs in addition to the electromagnetic calorimeter a hadronic calorimeter with a wide geometric coverage and good resolution.

The detector is structured like an onion. In the inner most layer, a tracker is built as close to the intersection point as possible to reconstruct the trajectories of charged particles. The precise reconstruction of tracks is important to the measurement of the particle momenta and the clustering of jets. This precise measurement of the trajectories allows a good resolution of secondary vertices and therefore makes it possible to identify jets arising from the hadronization of  $b$ -quarks. This is due to hadrons containing  $b$ -quarks have sufficient lifetime that they travel a certain distance before decaying.

The material of the tracking system has to fulfill three requirements to be suitable for the LHC.

First, the granularity of the tracker has to be high to achieve a good resolution on the trajectories. Secondly, because of the high event rate and high amount of pileup at the LHC, the response time of the modules have to be low. Thirdly, the material has to be able to withstand a high amount of radiation. The last part is even more important for an electron-positron collider, because radiative losses via Bremsstrahlung ( $\propto \frac{1}{m^4}$ ) are higher for electrons than for protons ( $m_p \approx 2000 \cdot m_e$ ) [13]. For these reasons, a silicon-based technology was used. The complete system covers the space of pseudo rapidity<sup>2</sup>  $|\eta| \leq 2.5$ . Closest to the beampipe is a pixel detector which has a high resolution and allows the measurement of secondary vertices. After this, a strip detector is implemented which has a lower resolution but is not as expensive. The next layer consists of the electromagnetic calorimeter (ECAL). Its purpose is to measure the energy deposition of electrons and photons. The electrons and photons produce electromagnetic showers. The energy of photons produced in these showers can be measured with photomultipliers. After this, the hadronic calorimeter (HCAL) measures the energy deposition of the particles that mostly interact via the strong force. The material of this part has to be dense because of the energy loss dependency in the Bethe-Bloch equation ( $dE/dx \propto \rho$ )[13]. This set of calorimeters is placed in three areas. One area is a cylindrical shape parallel to the beampipe and is called barrel. The other 2 areas are called endcaps and are placed at the beginning and at the end of the barrel.

Due to the fact that muons can pass the electromagnetic and hadronic calorimeters almost without loosing energy, an outer tracker is needed. This outer tracker is called the muon system. All these layers are immersed in a homogeneous field of a solenoid, placed between the calorimeter and muon systems, with a strength of 3.8 T. This makes it possible to determine the momentum of electrically charged particles by the curvature of their trajectories. In figure 2.2 a complete overview of the detector is given.

The standard coordinate system used by CMS is a zylindric coordinate system with the beam axis parallel to the z-axis. The angle perpendicular to the beam axis is called  $\phi$  while the angle  $\theta$  parallel to the beam axis is replaced by the pseudo rapidity  $\eta = -\ln(\theta/2)$ . The pseudo rapidity is prefered over  $\theta$  in pp-collisions due to the invariance to Lorentz boosts.

---

<sup>2</sup>Definition later in this section.

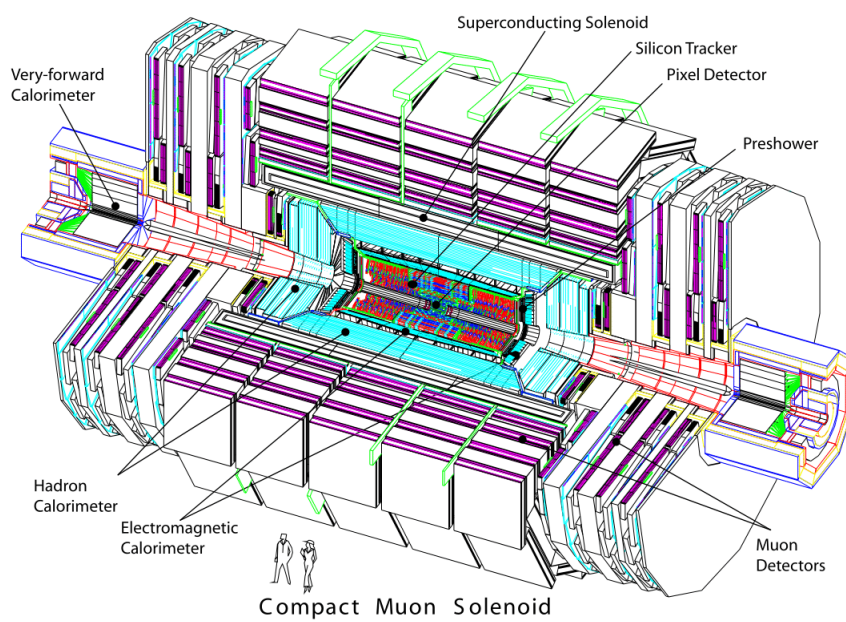


Figure 2.2: Overview of the Compact Muon Solenoid detector (taken from ref. [3]).

# Chapter 3

## Methods

### 3.1 General information on the analysis

The goal is to get a di-jet mass (missing mass) distribution that is most likely to represent the distribution that would be obtained with a real measurement at 240 (350) GeV. To achieve this all the relevant signal and background processes have to be generated. In figure 3.1 the most important processes and their cross sections are shown. All these processes have different kinematics which can be used to discriminate background events and favor signal events. In this way distributions can be achieved in which the signal process and background process are for the most part separated. This separation can be further improved by using the known constraints of the reaction to scale the events.

#### 3.1.1 Event generation

To generate the Monte Carlo (MC) event samples PYTHIA 8.212 is used [14][15]. PYTHIA offers sample main programs to simplify the event generation. In this analysis, the sample program main03.cc is used<sup>1</sup>. The following processes are used for signal and background generation<sup>2</sup>:

- Higgsstrahlung: HiggsSM:ffbar2HZ
- VBF: HiggsSM:ff2Hff(t:WW)
- ZZ: WeakDoubleBoson:ffbar2gmZgmZ, WeakZ0:gmZmode = 2

---

<sup>1</sup>A main03.cmnd example file for the Higgsstrahlungs process can be found in the appendix A.

<sup>2</sup>The syntax is as documented in the PYTHIA 8 manual [16].

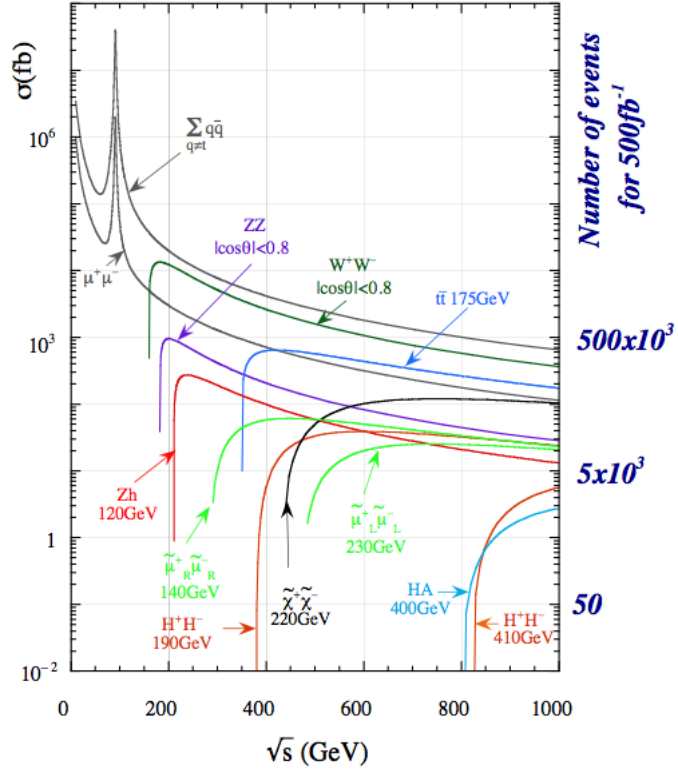


Figure 3.1: Cross sections for different processes and different center of mass energies (taken from ref. [4]).

Table 3.1: Number of generated events for each process.

Process	Events generated (240 GeV)	Events generated (350 GeV)
Higgsstrahlung	500 000	500 000
VBF	100 000	100 000
ZZ	1 000 000	500 000
WW	1 000 000	1 000 000
$q\bar{q}$	7 000 000	2 000 000

- WW: WeakDoubleBoson:ffbar2WW
- $q\bar{q}$ : WeakSingleBoson:ffbar2ffbar(s:gmZ)

For the  $q\bar{q}$  background the virtual  $Z/\gamma$  boson is forced to decay into quarks. The number of generated events are shown in table 3.1 and the cross sections are displayed in table 3.2.

### 3.1.2 The FCC software

For this analysis the software heppy<sup>3</sup> is used to process the generated events. This software is based on python and was mostly developed by Colin Bernet.

To simulate a real detector heppy uses the papas software which comes from the same repos-

<sup>3</sup>The software can be found in the FCC Github [17].

Table 3.2: Cross sections for signal and the most important backgrounds for the missing energy channel at 240 GeV and 350 GeV [6][4].

Process	$\sigma$ [pb] (240 GeV)	$\sigma$ [pb] (350 GeV)
$e^+e^- \rightarrow Z^* \rightarrow HZ$	0.19	0.135
$e^+e^- \rightarrow H\nu\bar{\nu}$ (WW-fusion)	0.007	0.027
$e^+e^- \rightarrow Z^*/\gamma^* \rightarrow q\bar{q}$	50	6
$e^+e^- \rightarrow W^+W^-$	16	3
$e^+e^- \rightarrow ZZ$	1.3	0.3

itory. The parameters for the detector are choosen to emulate the CMS detector described in section 2.3. All parameters can be found in `heppy/papas/detectors/CMS.py`<sup>4</sup>. The parameters from the original CMS.py were tuned to emulate the insitu performance of the real CMS detector. The CMS.py is almost unchanged used as the base for this analysis. The tracker efficiency is improved from 95% efficiency for  $|\eta| \leq 1.35$  and  $p_T \geq 500$  MeV to 100% efficiency for  $|\eta| \leq 1.74$  and  $p_T \geq 200$  MeV. The reason for this change is that a much more efficient tracker can be used at  $e^+e^-$ -collider than at pp collider because it is possible to get closer to the interaction point. This change allows the comparison of the results to [6]. This detector will be referred to as CMS and is used for the generation of all plots if not explicitly mentioned otherwise. The default values of the most important parameters are as follows:

- Electromagnetic calorimeter energy resolution (barrel)  $\approx \frac{0.04}{\sqrt{E}} \oplus \frac{0.16}{E} \oplus 0.007$
- Hadronic calorimeter energy resolution (barrel)  $\approx \frac{0.81}{\sqrt{E}} \oplus \frac{2.75}{E} \oplus 0.15$
- Tracker efficiency: 100% for  $|\eta| \leq 1.74$  and  $p_T \geq 200$  MeV. 90% for  $|\eta| \leq 2.5$  and  $p_T \geq 500$  MeV.
- Tracker radius: 1.29 m.
- Magnetic field: 3.8 T.
- Transverse momentum resoloution = 1.1%

The original CMS.py will be referred to as in-situ CMS. The only difference between the in-situ CMS and CMS is the tracking efficiency. For the in-situ CMS the tracking efficiency is 95% for  $|\eta| \leq 1.35$  and a  $p_T \geq 500$  MeV and 90% for  $|\eta| \leq 2.5$  and  $p_T \geq 500$  MeV. To reproduce the results from [18] two more detectors are studied. In the article [18] the International Linear Detector (ILD) [5] and a variation of the CMS detector are compared. The tracking efficiency

<sup>4</sup>Exact code can be found in the appendix B.

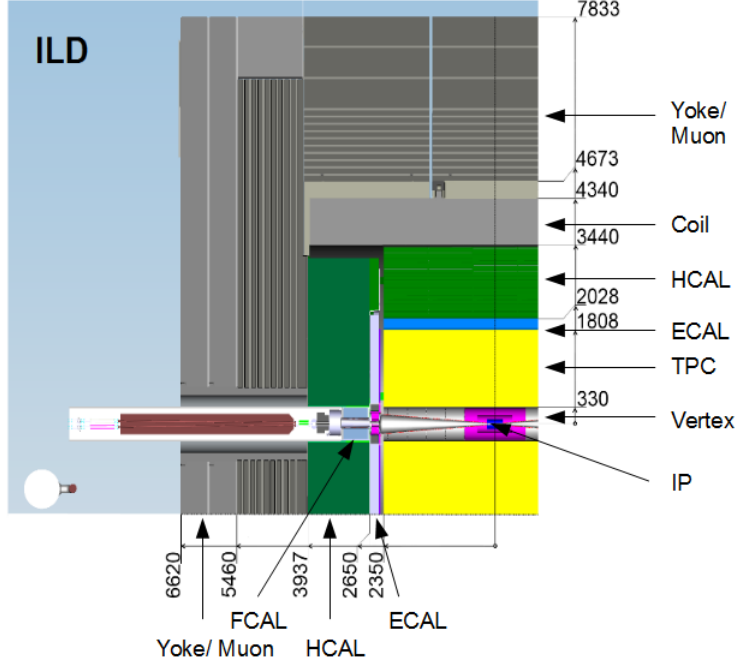


Figure 3.2: Overview of the overall dimension [mm] of the ILD (taken from ref. [5]).

for CMS in [18] is 95% for particles with  $|\eta| \leq 2.4$  and  $p_T \geq 100 \text{ MeV}$  and the  $p_T$  resolution is 3%. This variation of the CMS detector will be referred to as  $\widehat{\text{CMS}}$ . The ILD is one of two detectors designed for the International Linear Collider (ILC), a future linear  $e^+e^-$ -collider. To get an approximation of the ILD detector the parameters in CMS.py are changed according to the technical design report volume 4 [5], the card file from the delphes github [19] and from [18]. The most important parameters for the ILD detector are the following:

- Electromagnetic calorimeter energy resolution (barrel+endcap)  $\approx \frac{0.153}{\sqrt{E}} \oplus 0.0106$
- Hadronic calorimeter energy resolution (barrel+endcap)  $\approx \frac{0.5}{\sqrt{E}} \oplus 0.015$
- Tracker efficiency: 99% for  $|\eta| \leq 2.4$  and  $p_T \geq 100 \text{ MeV}$
- Magnetic field: 3.5 T.
- $p_T$  dependent transverse momentum resolution between 0.1% and 1%.

The overall dimensions of the ILD detector are taken from figure 3.2.

### 3.1.3 *b*-tagging

The *b*-tagging is essential for this analysis as the final state  $b\bar{b} + E_{miss}$  is studied. The jet clustering is done by the  $k_t - ee$ -algorithm which is a modified version of the  $k_t$ -algorithm [20]

and is adjusted to the coordinate system at a  $e^+e^-$ -collider, i.e.  $\theta/\phi$  coordinates. The algorithm is forced to form 2 jets. Events with less than 2 reconstructed particles are discarded. At first, the jets on truth level (genjets) are matched with the particles on truth level (genparticles) which are coming directly from the hard process. The particles coming from the hard process get identified by Status=23 as they get marked with this number by PYTHIA [21], which is the official convention for MC as documented by the Particle Data Group (PDG). After that, the genjets are matched with the reconstructed jets resulting from papas<sup>5</sup>. Two objects are matched if the following condition is met:

$$dR = \sqrt{\Delta\phi^2 + \Delta\theta^2} \leq 0.5 \quad (3.1)$$

$\phi$  is the angle perpendicular to the beam axis while  $\theta$  is the one parallel to it. If more than one object fulfills equation 3.1 only the one with the smallest dR is matched.

To be able to compare the results with [6] a  $b$ -tagging efficiency of 93% for jets that are matched with a  $b$ -quark is chosen. The corresponding misidentification rates for  $c$ -quarks (20%) and  $u$ -,  $d$ -,  $s$ -quarks/gluons (2%) that got matched with a jet are taken from a study for a future linear  $e^+e^-$ -collider [22].

To improve the MC statistic the events are weighted, instead of cut out, with the  $b$ -tag probability. This weighting is especially important for the backgrounds as the efficiency of these processes is supposed to be low. In figure 3.3 the impact of this weighting on the WW background is shown.

## 3.2 The missing energy channel at 240 GeV

### 3.2.1 Event selection

The selection is performed on the reconstructed jets. The goal is to select events arising from Higgsstrahlung and VBF with the final state  $\nu\bar{\nu}(H \rightarrow b\bar{b})$  and reject events resulting from all other processes (background). The characteristics of this final state are 2 jets arising from  $b$  quarks and a significant amount of missing energy. The most important backgrounds and their cross section are listed in table 3.2.

To select signal events (Higgsstrahlung + VBF) and suppress the backgrounds (ZZ +  $q\bar{q}$  + WW)

---

<sup>5</sup>See Section 3.1.2.

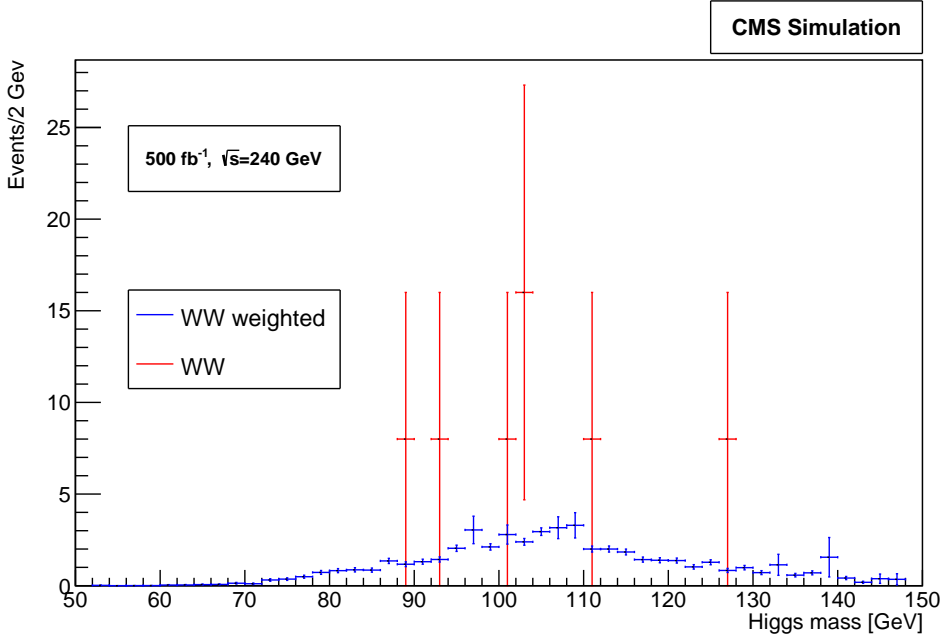


Figure 3.3: Impact of the  $b$ -tagging weights on the statistics of the WW background after the event selection (see section 3.2.1). The di-jet mass is on the x-axis.

the exact same selection requirements as those in [6]<sup>6</sup> are used. Events with 2 b-jets are selected. Because of the fact that at an  $e^+e^-$ -collider the total momentum has to be conserved, we can use the total missing energy instead of only the missing transverse energy as it is usually done at hadron colliders like LHC. The visible mass  $m_{vis}$  has to be between 10 GeV and 180 GeV while the missing mass  $m_{miss}$  is restricted to be between 65 GeV and 125 GeV. The visible Lorentz vector  $\mathbf{p}_{vis}$  is defined by the sum of the Lorentz vectors of all reconstructed particles ( $m_{vis}^2 = \mathbf{p}_{vis}^2$ ). The missing energy is defined as the difference between the center-of-mass energy and the sum of the energies of all reconstructed particles. The missing momentum is defined by the negative sum of the momenta of all reconstructed particles. Therefore the square of the resulting Lorentz vector defines the missing mass. The total momentum transverse to the beam axis  $p_T$  has to be higher than 15 GeV while the total longitudinal momentum  $p_L$  is required to be below 50 GeV. To reduce the ZZ and WW background the acollinearity  $\Theta$ , defined as the angle between the two jets, is required to be above 100 degrees. To reduce the  $q\bar{q}$  background the following variable has to be above 10.

$$\text{cross} = \frac{180}{\pi} \cdot \arcsin\left(\frac{(\vec{p}_{jet1} \times \vec{p}_{jet2}) \cdot \hat{e}_z}{|\vec{p}_{jet1}| \cdot |\vec{p}_{jet2}|}\right) \quad (3.2)$$

$\vec{p}_{jet1}$  and  $\vec{p}_{jet2}$  are the momentum vectors of the two reconstructed jets. Table 3.3 displays the

<sup>6</sup>The exact selection requirements are not described in [6], which is why they are coming from one of the articles authors (Patrick Janot)

Table 3.3: Marginal selection efficiencies [%] for the different processes studied at 240 GeV.

Process	<i>b</i> -tag	$m_{vis}$	$m_{miss}$	$p_T$	$p_L$	$\Theta$	cross	Total efficiency
Higgsstrahlung	39.6	100	75	99	97.5	99.9	72.5	4.3
VBF	50.2	100	73.2	98.7	91.1	99.9	71.8	16.7
$q\bar{q}$	7.8	100	40.1	98	99.9	100	1.6	0.001
ZZ	11.5	100	56.3	99.8	64.2	73.7	83.4	0.9
WW	0.03	100	51.7	99.8	69.1	56.2	78.7	0.001

marginal selection efficiency for the signal and background processes. The marginal selection efficiency for one cut is defined by the ratio of the number of events after all cuts to the number of events after all cuts except the marginal one.

### 3.2.2 Scaling

To normalize the histograms of the different processes to the same amount of integrated luminosity each histogram is scaled by a factor  $\kappa$  determined by the following equation:

$$\kappa = \frac{\mathcal{L}_{int} \cdot \sigma}{N} \quad (3.3)$$

$\mathcal{L}_{int}$  is the integrated luminosity,  $\sigma$  is the cross section and  $N$  is the number of generated events listed in table 3.1. An integrated luminosity of  $500 \text{ fb}^{-1}$  is assumed.

To improve the visible mass resolution of the signal the fact that for Higgsstrahlung a Z boson decays into two neutrinos is used. The two jet energies are rescaled by a common factor  $\alpha$  such that the constraint  $m_{miss}^{rescaled} = m_Z$  is satisfied.

$$m_Z^2 = (\mathbf{p}_{miss}^{rescaled})^2 \quad (3.4)$$

$$\mathbf{p}_{miss}^{rescaled} = (0, 0, 0, \sqrt{s})^T - (\alpha \mathbf{p}_1 + \alpha \mathbf{p}_2) \quad (3.5)$$

$$\alpha_{1,2} = \frac{E_{vis} \cdot \sqrt{s}}{m_{vis}^2} \pm \sqrt{\left(\frac{E_{vis} \cdot \sqrt{s}}{m_{vis}^2}\right)^2 - \frac{\sqrt{s}^2 - m_Z^2}{m_{vis}^2}} \quad (3.6)$$

$\mathbf{p}_1$  and  $\mathbf{p}_2$  denote the four-vectors of the two jets and  $\sqrt{s}$  is the center of mass energy. Only the smaller solution for  $\alpha$  ( $\pm \rightarrow -$ ) is used as the other solution results in unphysical outcomes.

In figure 3.4 the impact of this scaling on Higgsstrahlung and VBF is shown. In figure 3.5 the di-jet mass distribution after the event selection and scaling is shown. This distribution is qualitatively the same as in [6] and therefore enhances the credibility of this analysis.

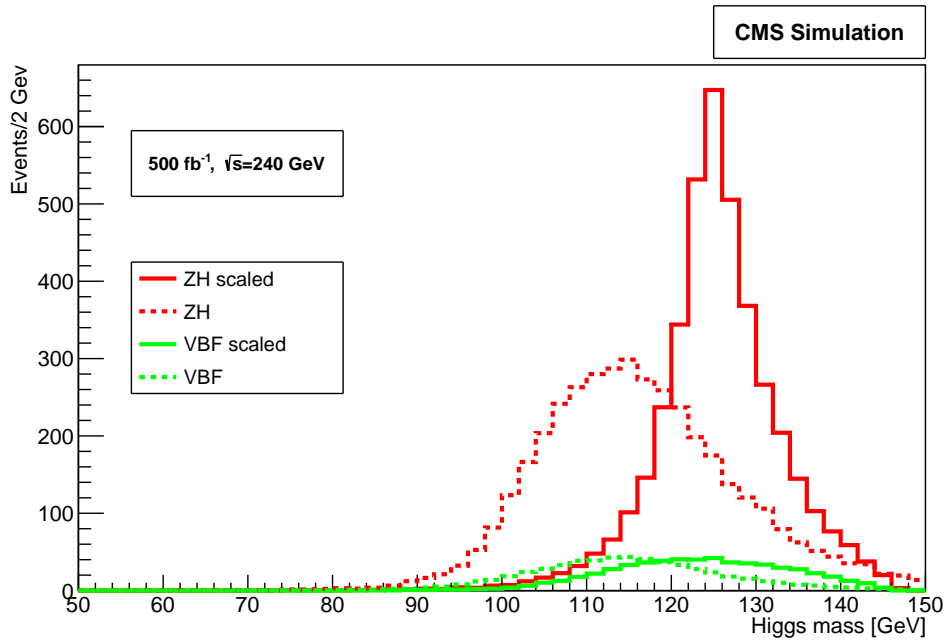


Figure 3.4: The mass of the reconstructed  $b$ -jets before and after scaling for Higgsstrahlung and VBF (after event selection).

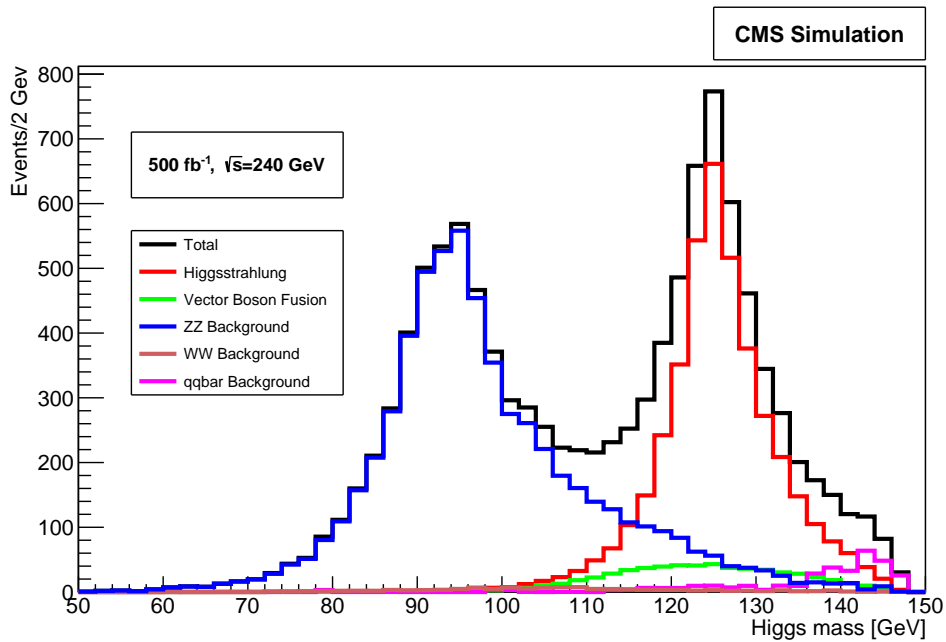


Figure 3.5: Di-jet mass distribution for  $500 \text{ fb}^{-1}$  and  $240 \text{ GeV}$  after event selection and scaling.

### 3.3 The missing energy channel at 350 GeV

At 350 GeV the cross section for VBF production  $\sigma_{VBF}$  and  $\sigma_{HZ} \times BR(Z \rightarrow \nu\bar{\nu})$  are both at 27 fb (see figure 1.1). For this reason a precise measurement of  $\sigma_{VBF} \times BR(H \rightarrow b\bar{b})$  is possible. Instead of looking at the di-jet mass it is beneficial to study the missing mass distribution as the Higgsstrahlungs process peaks at  $m_{miss} \approx m_Z$  while for VBF the peak is at around  $m_{miss} \approx \sqrt{s} - m_H$ . This gives a better separation of signal and background as now only VBF is the signal.

#### 3.3.1 Event selection

In figure 3.1 the cross sections for  $e^+e^-$ -collisions at different  $\sqrt{s}$  are displayed. In table 3.2 the cross sections for the most important processes for 350 GeV are shown.

The event selection is based on [23] and is done on the reconstructed jets. The distribution for each constraint of the VBF process is examined and the boundaries for each constraint are optimized if necessary.

Events with two b-jets are selected. The visible mass  $m_{vis}$  is required to be between 80 GeV and 130 GeV. The visible energy  $E_{vis}$  has to be above 100 GeV and below 180 GeV. To further reduce the  $q\bar{q}$  background the acoplanarity  $\beta$ , defined as the angle between the jet plane and the beam axis, is required to be above 10 degrees. Also the total transversal momentum is required to be between 10 GeV and 140 GeV.

The marginal selection efficiencies are shown in table 3.4. The missing mass distribution for

Table 3.4: Marginal selection efficiencies [%] for the different processes studied at 350 GeV.

Process	b-tag	$m_{vis}$	$\beta$	$p_T$	$E_{vis}$	scaling	Total efficiency
Higgsstrahlung	44.3	96.9	86.7	99.9	93.7	87.9	4.9
VBF	49.1	98.1	83.5	99.2	95.6	98.7	23.7
$q\bar{q}$	0.6	6.8	6.3	25	68.1	97.9	0.0001
$ZZ$	7.9	76.4	76.7	99.9	93.6	10.6	0.13
$WW$	0.02	86.3	64.8	99.9	60.3	35.8	0.0004

this event selection is shown in figure 3.6.

#### 3.3.2 Scaling

For the same reasons as in section 3.2.2 the scaling of equation 3.3 is applied.

Instead of constraining the missing mass, the visible mass is constrained to be at the higgs

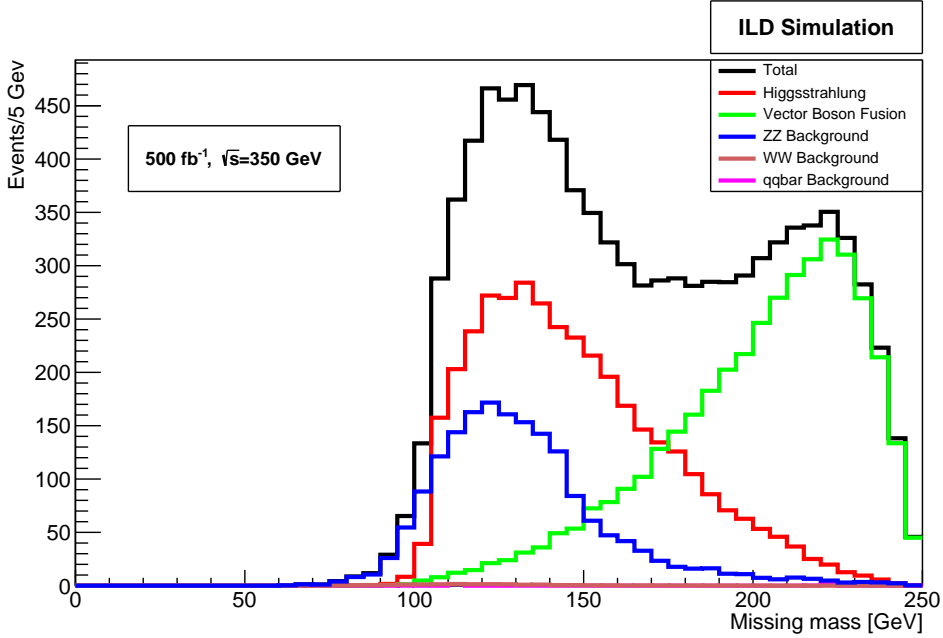


Figure 3.6: Missing mass distribution for  $500 \text{ fb}^{-1}$ ,  $\sqrt{s}=350 \text{ GeV}$  and the ILD detector after event selection.

mass  $m_{vis}^{rescaled} = m_H$ . This improves the resolution of the Higgsstrahlung and therefore allows a greater separation between background and signal (VBF). To fulfill this constraint the four-vectors of the two jets are scaled by a common factor  $\Upsilon$ :

$$\Upsilon = \frac{m_H}{m_{vis}} \quad (3.7)$$

The new missing mass  $m_{miss}^{rescaled}$  is now given by the following equation:

$$m_{miss}^{rescaled} = \sqrt{(\sqrt{s} - \Upsilon \cdot E_{vis})^2 - (\Upsilon \cdot \vec{p}_{vis})^2} \quad (3.8)$$

Events with negative  $(m_{miss}^{rescaled})^2$  are discarded. In figure 3.7 and 3.8 the missing mass distributions after event selection and scaling is displayed for the CMS and the ILD detector. The distribution from ILD is in good agreement with the distribution from [23]. The diminishing number of ZZ events are the result of the  $(m_{miss}^{rescaled})^2$  distribution shown in figure 3.9.

## 3.4 Statistical analysis

The goal of obtaining  $\sigma_{Signal} \times BR(H \rightarrow b\bar{b})$  can be achieved by measuring the uncertainty on the number of signal events  $\Delta N_{Signal}$ . Equation 2.1 shows that the errors are the same, ignoring a small influence of the uncertainty on the integrated luminosity. To determine the uncertainty

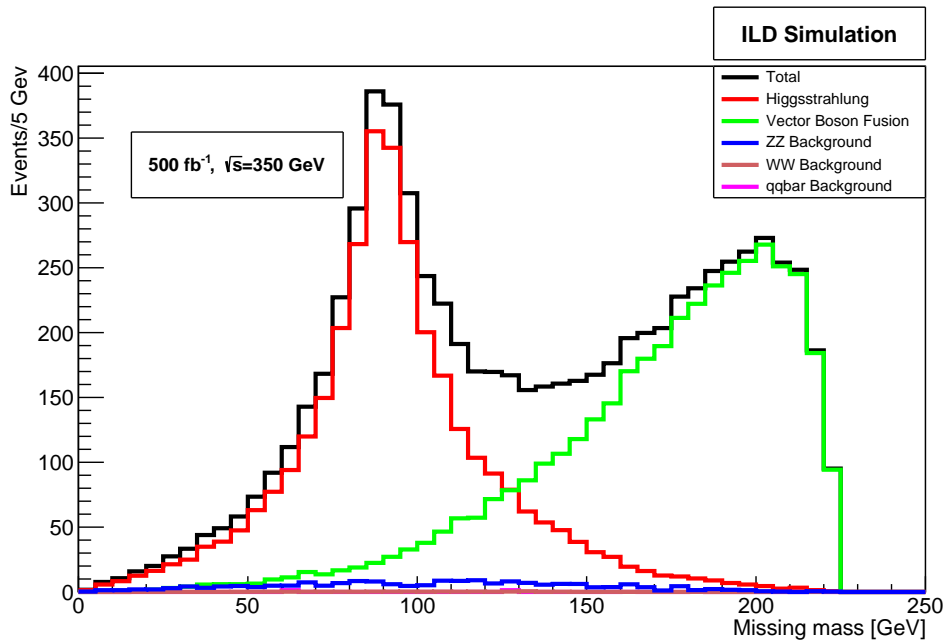


Figure 3.7: Missing mass distribution at 350 GeV after scaling and event selection for  $500 \text{ fb}^{-1}$  and the ILD detector.

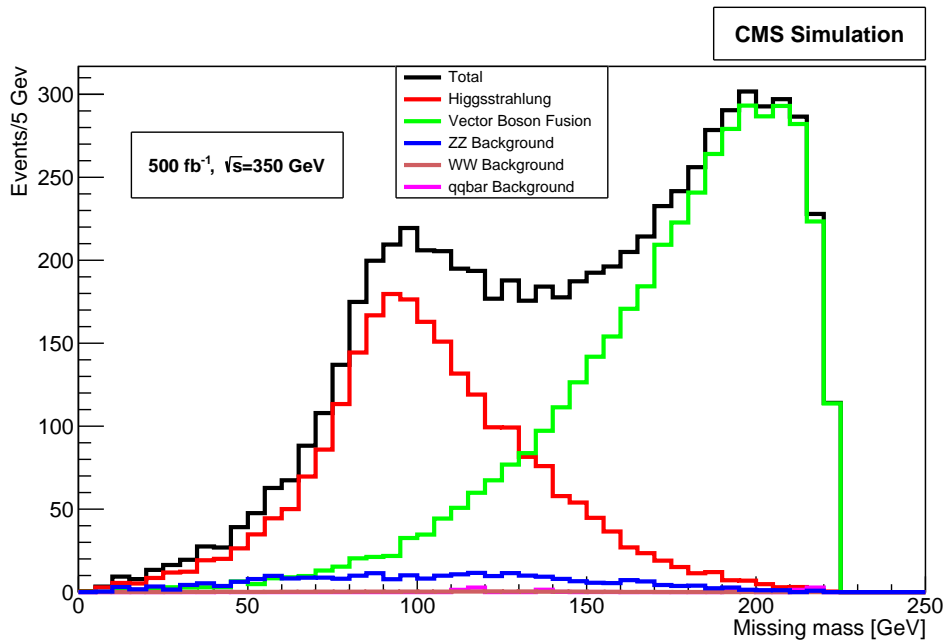


Figure 3.8: Missing mass distribution at 350 GeV and  $500 \text{ fb}^{-1}$  after scaling and event selection for the CMS detector.

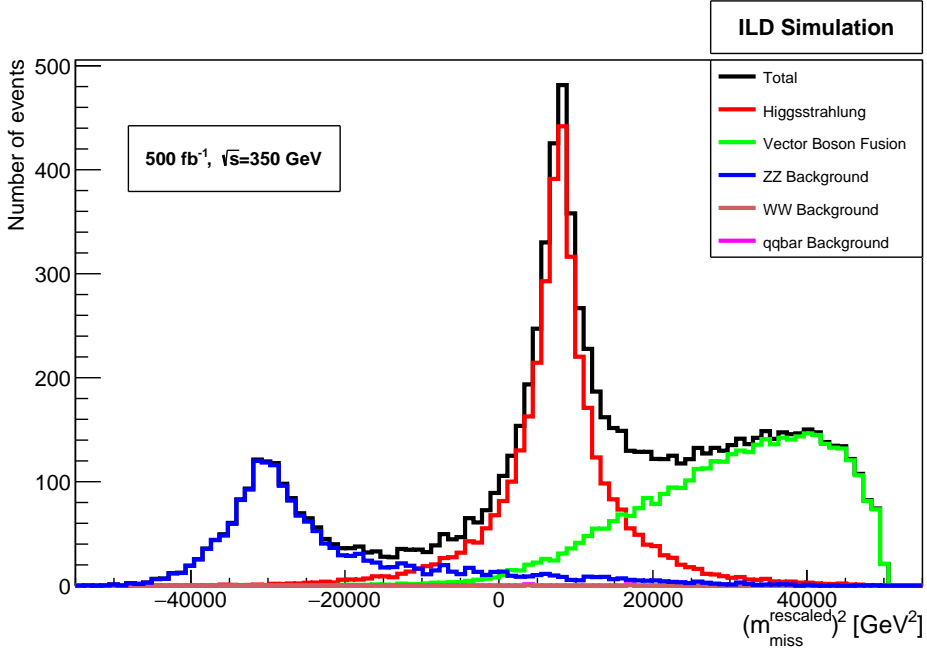


Figure 3.9:  $(m_{miss}^{rescaled})^2$  distribution after event selection with the ILD detector for 350 GeV and  $500 \text{ fb}^{-1}$ .

on  $\sigma_{VBF+HS} \times BR(H \rightarrow b\bar{b})$  at 240 GeV the di-jet mass distribution is examined. At 350 GeV the missing mass distribution is studied to calculate the uncertainty on  $\sigma_{VBF} \times BR(H \rightarrow b\bar{b})$ . At 240 GeV the signal (VBF + ZH) is fitted with the sum of a gaussian and a Lorentz distribution while the background is fitted by the sum of a crystalball and a gaussian. At 350 GeV the signal (VBF) is fitted to a gaussian whereas the background is fitted to the sum of a gaussian and a Lorentz distribution. The fitting is done with ROOT [24] which uses the Minuit [25] minimizer. The fits performe a  $\chi^2$  minimizing alogrithm. the  $\chi^2$  is defined as follows:

$$\chi^2 = \sum_i \frac{(x_{i,observed} - x_{i,predicted})^2}{\sigma_{i,observed}^2} \quad (3.9)$$

The sum goes over all bins. The goodness of a fit is evaluated by the reduced  $\chi^2_{reduced}$ :

$$\chi^2_{reduced} = \frac{\chi^2}{n_{NDF}} \quad (3.10)$$

$n_{NDF}$  is the number of degrees of freedom and is defined as the number of points in the fit subtracted by the number of free parameters.

The  $\chi^2_{reduced}$  after minimization and fit ranges are shown in table 3.5. The fact that the  $\chi^2_{reduced}$  are close to 1 means that the fit functions describe the distributions well. The FCC-ee project is planed to run at 91 GeV, 161 GeV, 240 GeV and 350 GeV [1]. So before the run at 240 GeV

Table 3.5: Fit ranges and the resulting  $\chi^2_{reduced}$  for 240 GeV and 350 GeV fits.

Fit	Fit range	$n_{NDF}$	$\chi^2_{reduced}$
240 GeV			
Signal fit	110-140	6	1.1
Background fit	70-140	8	0.9
Total fit	70-140	7	0.9
350 GeV			
Signal fit	50-205	3	0.9
Background fit	50-205	6	1.3
Total fit	50-205	4	1.1

the Z-pole measurement ( $\sqrt{s} \approx 90$  GeV) will already be done and allow the simulations to describe the shape of the ZZ background at 240 GeV very well. Same argument goes for the analysis at 350 GeV where the shape of the Higgsstrahlung distribution will be well known due to the run at 240 GeV. For this reason the shape of the background is determined by a fit on the histogram containing all backgrounds. The total histogram is fitted with the signal plus background function where the background shape is fixed and only the yield is fitted.

To determine the uncertainty of  $\sigma \times BR(H \rightarrow b\bar{b})$  the uncertainty on the integral of the signal function has to be calculated. This calculation is done with two different methods. The idea of the first method is to simulate measurements based on the original histogram (see section 3.4.1) while the other uses the gaussian approximation for propagation of uncertainty (see section 3.4.2).

### 3.4.1 Poisson smearing

One method to determine the precision of  $\sigma_{Signal} \times BR(H \rightarrow b\bar{b})$  is to use the histogram from the MC simulation and change the content of every bin randomly based on a Poisson distribution with a mean of the bin content and fit the total fit function again. The problem with this way is that due to the complexity of the fit function the reduced  $\chi^2$  of a fit on a histogram that is smeared with the Poisson distribution is on average at 1.5. This means that most of the new histograms are not well described by the fit function. To solve this problem the method is adjusted. Instead of smearing the histogram from MC simulation a Poisson smeared histogram from the fit function of the original MC histogram is created. This way the reduced  $\chi^2$  is per definition equal to one. Figure 3.10 shows the distribution of the reduced  $\chi^2$ . For each analysis  $T=100000$  histograms are generated by setting the bin content to a value randomly chosen from a Poisson distribution with a mean of the fit function value at the bin position. The errors of

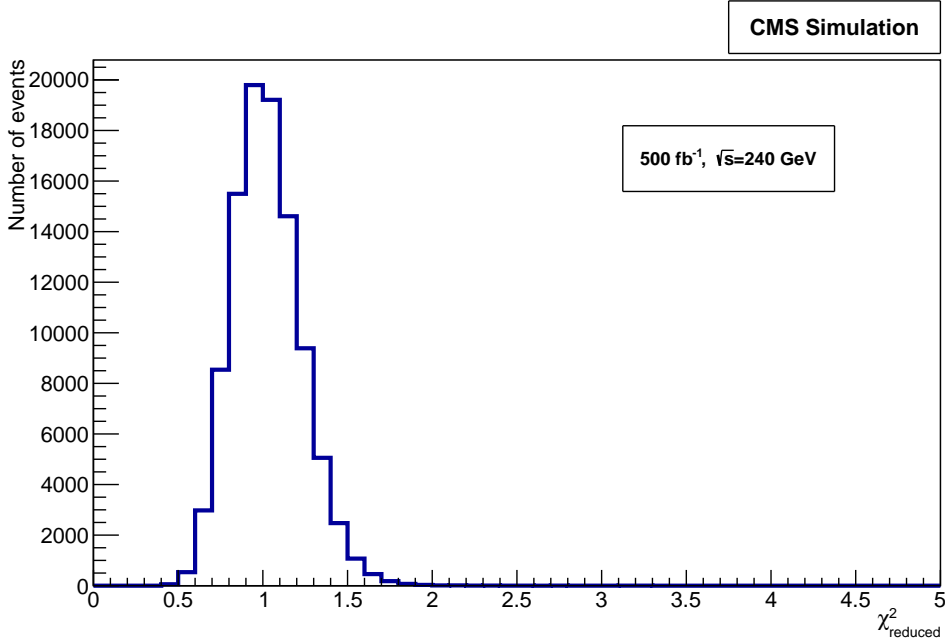


Figure 3.10: Reduced  $\chi^2$  distribution for functions fitted to the histogram resulting from the fit function.

every bin are set to the square root of their content as it would be the case in a real measurement. On each histogram the total fit function is fitted and the integral of the signal function, which is a part of the total fit function, is calculated in the range of the total fit (see table 3.5). The histograms in which the minimization is not successful are discarded. Total number of generated histograms in which the minimization failed is denoted as  $T_{failed}$ . In approximately 1 out of 100 generated histograms does the minimization fail. With this procedure<sup>7</sup> the resulting distribution of the signal yield is shown in figure 3.11.

The error is given by the standard deviation of the distribution in 3.11 defined by the following equation:

$$\Sigma = \sqrt{\frac{1}{T - T_{failed}} \sum_i (S_i - S_{mean})^2} \quad (3.11)$$

$S$  is the integral over the signal function. Assuming that the error on  $\Sigma$  and the error on the signal yield  $S$  are uncorrelated, the error of the relative error can be calculated by the following formula:

$$\sigma_{\frac{\Sigma}{S_{mean}}} = \sqrt{\left(\frac{\sigma_\Sigma}{S_{mean}}\right)^2 + \left(\frac{\Sigma}{S_{mean}}\right)^4} \quad (3.12)$$

$\sigma_\Sigma$  is the standard deviation of the standard deviation and is calculated by the ROOT function `TH1::GetStdDevError()`. In figure 3.12 the dependency of  $\sigma_{\frac{\Sigma}{S_{mean}}}$  on the number of generated histograms is shown.

<sup>7</sup>This process takes approximately 15 minutes.

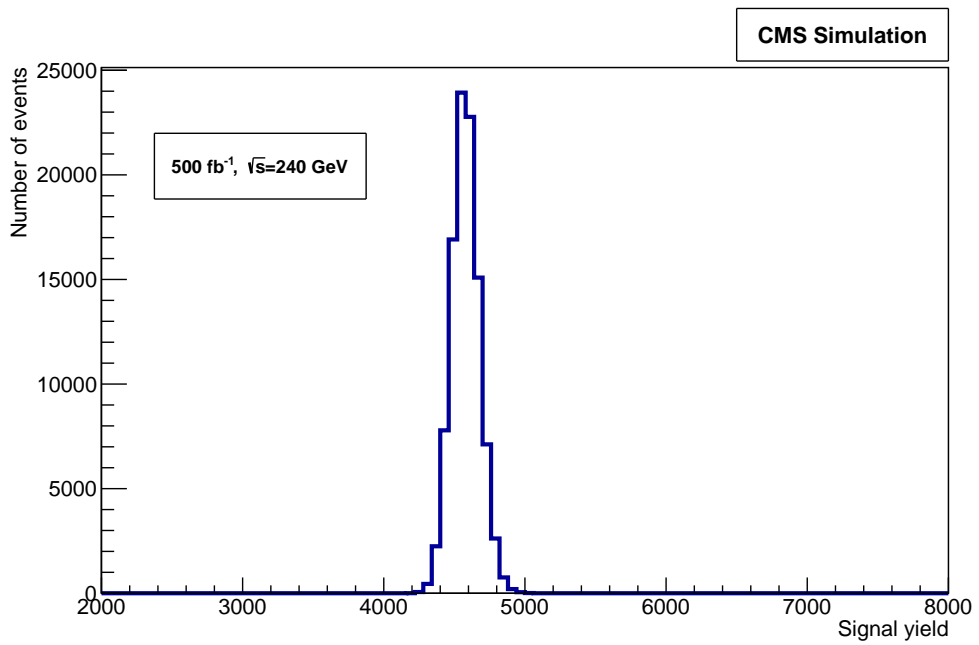


Figure 3.11: Signal yield distribution for 240 GeV and  $500 \text{ fb}^{-1}$ .

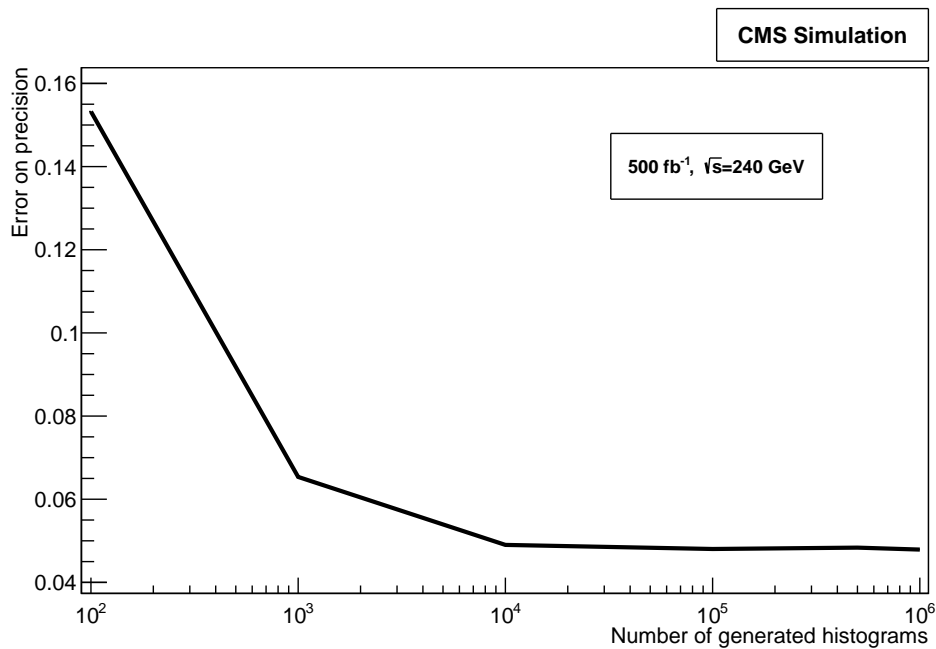


Figure 3.12: Behavior of the error on the uncertainty (equation 3.12).

### 3.4.2 Gaussian propagation of uncertainty (POU)

To calculate the uncertainty on the signal yield the covariance matrix of the total fit can be used. Before the total fit is done the errors of each bin in the total histogram are set to the square root of their content. The ROOT function `TF1::IntegralError()` is used to determine the uncertainty of integral over the signal function. The sub covariance matrix of the signal parameters (6x6 at 240 GeV, 3x3 at 350 GeV) and the signal function with the parameters from the total fit are given to the `IntegralError()` function as parameters. The calculations of this ROOT function are based on the following formula for the propagation of uncertainty in matrix expression [26]:

$$\sigma_f^2 = \mathbf{g}^T \mathbf{V} \mathbf{g} \quad (3.13)$$

$\sigma_f^2$  denotes the variance of a function  $f$  depending on parameters  $\beta_i$ .  $\mathbf{V}$  is the covariance matrix of  $f$  and  $\mathbf{g}$  is the vector with  $\partial f / \partial \beta_i$  as its elements.

# Chapter 4

## Results

### 4.1 Detector comparison

The four different detector designs described in section 3.1.2 are compared using the statistical methods described in section 3.4 for 240 GeV. The following are the most important characteristics of these detector designs:

- In-situ CMS: Tuned to reproduce real measurements of the CMS detector.
- $\widehat{CMS}$ : In-situ CMS with improved tracking efficiency and worse  $p_T$  resolution
- CMS: In-situ CMS with even better tracking efficiency than  $\widehat{CMS}$ .
- ILD: ILD detector based on predicted performance.

The results are shown in figure 4.1. The ILD achieves a higher precision than all the CMS variations. The in-situ CMS design has the worst precision with  $\approx 3.3\%$ . This plot also shows that the two statistical methods lead to roughly the same results and that the impact of the  $q\bar{q}$  and WW background negligible are. Table 4.1 shows the comparison of the results of this analysis with the CMS note [6]. If the background normalisation is also known, the precision increases by  $\approx 15\%$ . In [18] the ILD was compared with  $\widehat{CMS}$  and an increase of  $\approx 50\%$  in precision on the limit of  $BR(H \rightarrow \text{invis})$  was found for the ILD. The analysis presented in this thesis shows an increase of  $\approx 40\%$  for the precision of the  $\sigma_{HZ+VBF} \times BR(H \rightarrow b\bar{b})$  measurement for the same detector designs which is compatible with [18].

Three important factors influencing the  $\Delta N_{HZ+VBF} / N_{HZ+VBF}$  measurement are the core resolution, the signal over background ratio and the uncertainty on the background normalization

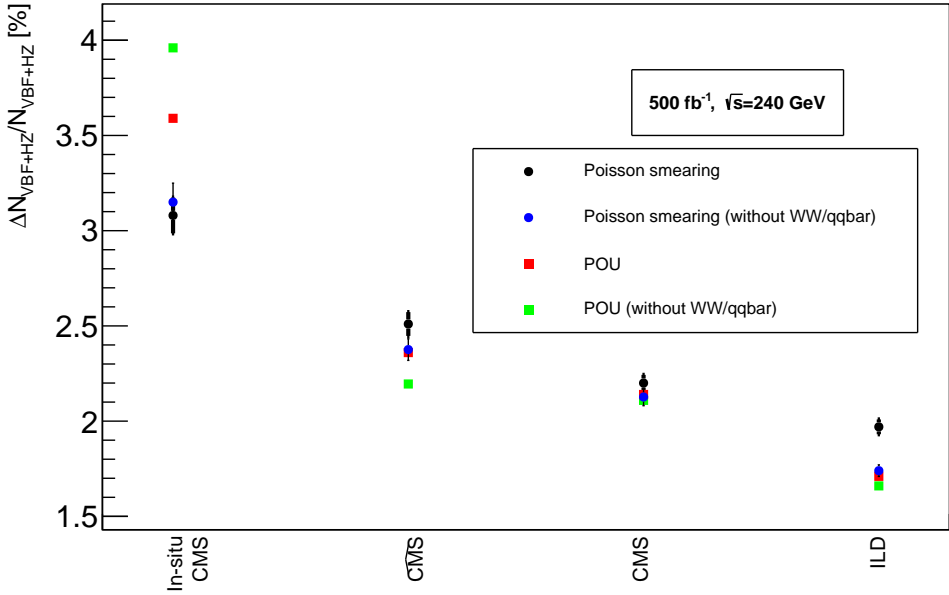


Figure 4.1: Precision achieved with the different detector designs. Poisson smearing and the propagation of uncertainty (POU) are used to obtain the precision. The blue and green points are obtained by a simulation with only Higgsstrahlung, VBF and ZZ.

Table 4.1: 240 GeV,  $\Delta N_{VBF+HZ}/N_{VBF+HZ}$  measurement [%] comparison with the CMS note [6] for the Poisson smearing and the propagation of uncertainty (POU) method.

Detector	Poisson smearing	POU	CMS note
In-situ CMS	$3.08 \pm 0.09$	3.59	/
$\widehat{CMS}$	$2.51 \pm 0.06$	2.36	/
CMS	$2.2 \pm 0.04$	2.14	1.8
ILD	$1.97 \pm 0.04$	1.71	/

factor. The core resolution  $r$  is defined as follows:

$$r = \frac{FWHM}{2.335} \quad (4.1)$$

FWHM denotes the full width at half maximum. For each of the 100000 histograms (see section 3.4.1) the core resolution of the signal function is calculated and stored in a histogram. From this histogram the mean is used for the core resolution plot. The signal over background ratio is obtained by dividing the signal histogram and background histogram bin by bin and integrating over all the bins. The binning of the dijet mass plot is changed to a total of 100 bins for this procedure. This simplifies the calculation of the signal yield. In figures 4.2-4.4 these three parameters are displayed.

A variable representing the jet resolution can be defined in the following way:

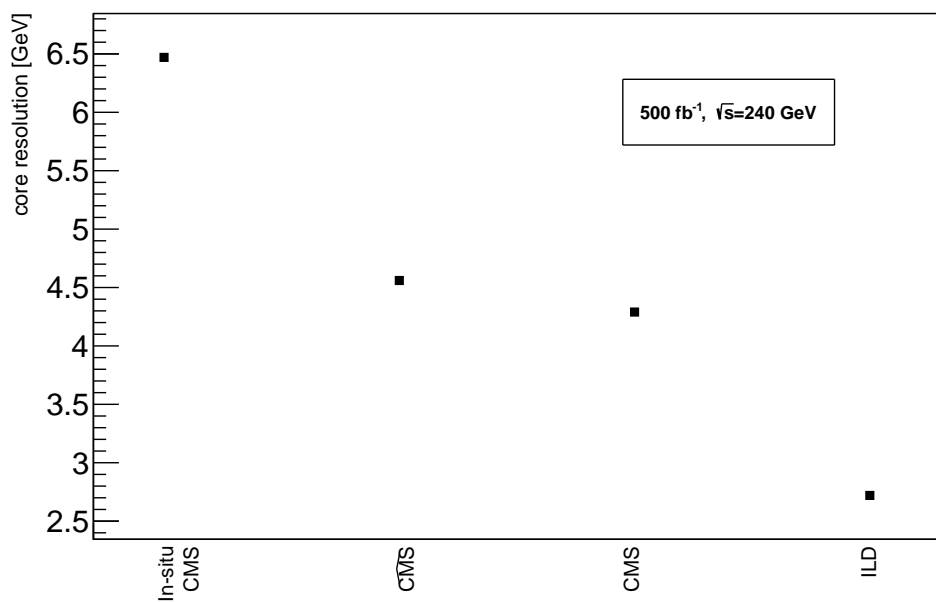


Figure 4.2: Core resolution of the signal function for the different detector designs.

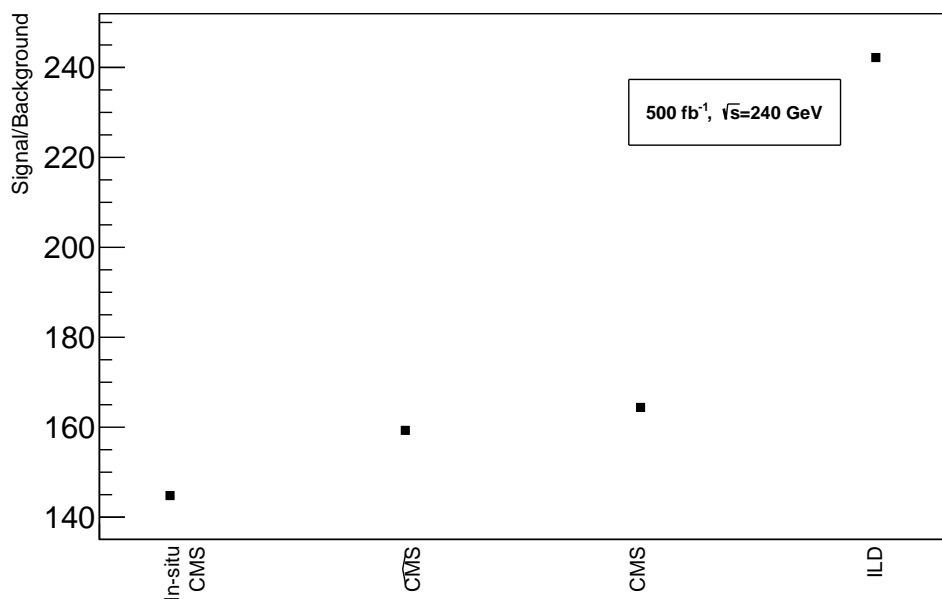


Figure 4.3: Signal over background for the different detector designs.

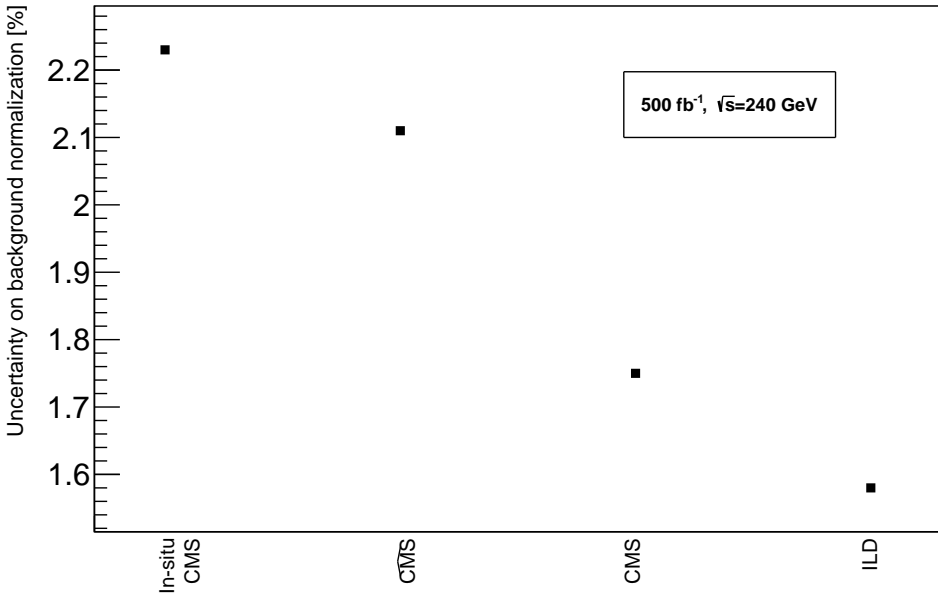


Figure 4.4: Uncertainty on the background normalization factor for the different detector designs.

$$\xi = \frac{E_{jet} - E_{genjet}}{E_{genjet}} \quad (4.2)$$

$E_{jet} - E_{genjet}$  is the energy difference between a reconstructed jet and the jet on truth level which is matched to it using the  $dR$  matching criterion defined in equation 3.1. In figure 4.5 the distribution of  $\xi$  from the leading jet of Higgsstrahlung is shown. For detectors with smaller core resolution the mean shifts to negative numbers while the standard deviation gets smaller. The fact that the standard deviation of the distribution for  $\xi$  is smaller for the ILD than for the CMS variations is a result of the better energy resolution of the calorimeters (see section 3.1.2). The shift explains why the peak of the missing mass for Higgsstrahlung in figure 3.6 is at 130 GeV instead of 91 GeV where it should be. The reason for this shift is not explicitly studied but is circumvented to a certain extent by the scaling (see sections 3.2.2 and 3.3.2). The effect on the event selection is not prevented. This problem could be solved by optimizing the event selection for each detector variation but that is not done in this analysis due to time constraints. Therefore, the impact of large changes in detector parameters might be underestimated.

The results for  $\sqrt{s} = 350$  GeV are shown in table 4.2. In [23] the uncertainty of  $\Delta N_{VBF}/N_{VBF}$

Table 4.2: 350 GeV,  $\Delta N_{VBF}/N_{VBF}$  measurement [%].

Detector	Poisson smearing	POU	two parameter fit
CMS	$6.6 \pm 0.4$	7.2	2.4
ILD	$4.3 \pm 0.2$	4.6	2.1

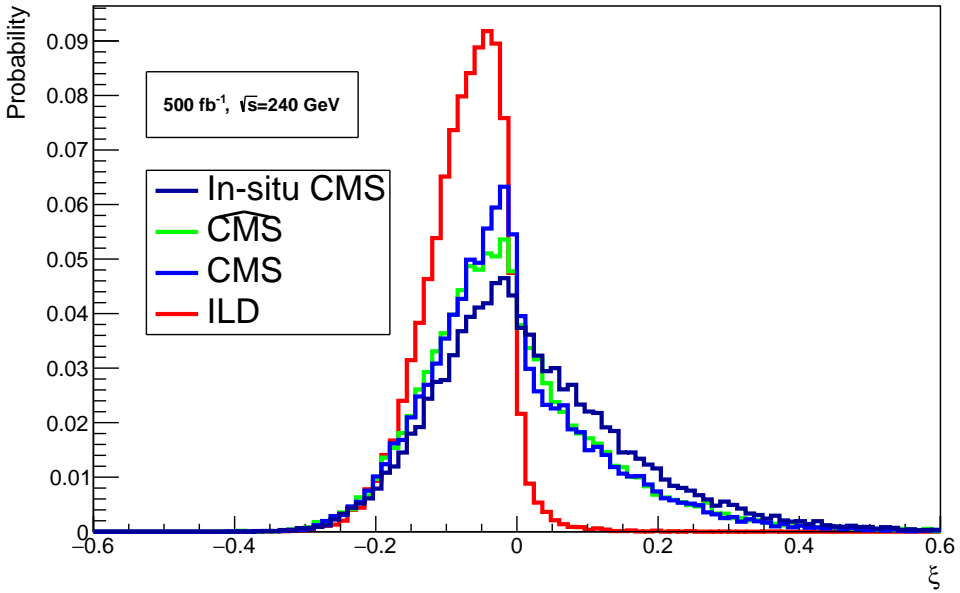


Figure 4.5: Distribution of  $\xi$  for the leading jet of Higgsstrahlung and different detector designs.

was determined by a fit with 3 free parameters. These 3 parameters correspond to the VBF yield, the Higgsstrahlungs yield and the number of background events. To be able to compare the results, a two-parameter fit is performed, where one parameter corresponds to the VBF yield while the other fits the background yield (Higgsstrahlung included). In ref. [23], an uncertainty of 2.6% for  $\Delta N_{VBF}/N_{VBF}$  and a Higgs boson mass of 130 GeV at 350 GeV and an integrated luminosity of  $500 \text{ fb}^{-1}$  was calculated. The analysis in [23] was done with a simulation of the TESLA detector [27] and because TESLA is designed for a linear  $e^+e^-$ -collider it is best to compare it to the ILD simulation. With the described two-parameter fit a precision of 2.1% for VBF and  $m_H = 125 \text{ GeV}$  is determined with the ILD simulation which is compatible with the results from [18]. [1] claims a precision of 0.6% with  $2.6 \text{ ab}^{-1}$  on  $\Delta N_{VBF}/N_{VBF}$ . With  $2.6 \text{ ab}^{-1}$  instead of  $500 \text{ fb}^{-1}$  the precision of the analysis presented in this thesis would increase from 2.1% to 0.9% with a two parameter fit which is compatible with [1].

## 4.2 Detector parameter impacts

To get a general overview of the impact of the parameters in the CMS detector on the precision of the measurement, only the signal is studied. This reduces the usage of computational capacities and allows for a faster evaluation of the results. For this purpose 100 000 events of Higgsstrahlung at 240 GeV are generated in which the Higgs decays into  $b\bar{b}$  and the Z boson into  $\nu\bar{\nu}$ . The resulting distribution is fitted with a gaussian and the width of this gaussian is

compared for different detector parameter choices. In table 4.3 the results of this method are displayed. Although the energy resolution of the electromagnetic calorimeter is not shown in table 4.3, it was studied and showed very little impact.

This way the three most impactful parameters are identified to be the tracker radius, the tracker

Table 4.3: Impact of different detector parameters on the width of the signal at 240 GeV. One parameter in the in-situ CMS simulation is changed by the given factor. The width is given by the standard deviation of a gaussian fitted to the signal. The cluster size determines the size of a cluster which is created if a particle gets measured.

Detector parameter	Factor	Width improvement [%]
Magnetic field	5/3.8	2.26
Tracker radius	1.8/1.29	3.89
Tracker efficiency	100%, $ \eta  \leq 2.5 \& p_T \geq 0.2$ GeV	20.99
ECAL cluster size	0.5	3.89
ECAL energy resolution	0.5	0.8
HCAL cluster size	0.5	0.86
HCAL energy resolution	0.5	21.49
$p_T$ resolution	0.5	0.1

efficiency and the energy resolution of the hadronic calorimeter. The tracker efficiency is the main difference between the different CMS variations and its effect has thus already been studied in the context of the comparisons between the three CMS detector variations above. The energy resolution of the hadronic calorimeter and the tracker radius are the biggest differences between the ILD and the CMS simulation as the tracking efficiencies are almost the same. For example, a jet with an energy of 100 GeV has a resolution of 17.27 (5.22) % for the CMS (ILD) simulation. The tracker radius is now looked upon in more detail.

The tracker radius of the CMS simulation is changed from 1.29 m to 2.04 m. The dimensions of all other detector elements (ECAL, HCAL, magnetic field) are changed accordingly. Figure 4.6 shows the results. The figure 4.6 shows a linear increase in precision from 1.29 m to 1.79 m. The increase from 1.79 m to 2.04 m is most likely a product of the shift in distributions as previously explained in section 4.1. The number of background events within the fit range increases from 6436 to 6578, which has a negative effect on the measurement.

To examine the effect of the energy resolution of the hadronic calorimeter, every term of the energy resolution ( $1/\sqrt{E}$ ,  $1/E$ , constant) in the barrel and the endcaps is changed by a factor  $\Omega$ . For this test only the signal and the ZZ background are simulated, so that the time required for the simulation is lowered. This has only a small impact on the results as it can be concluded from figure 4.1. Figure 4.7 shows the results of these changes. The improvement for  $\Omega = 0.25$  is most likely underestimated because 138 less signal events pass the event selection compared to

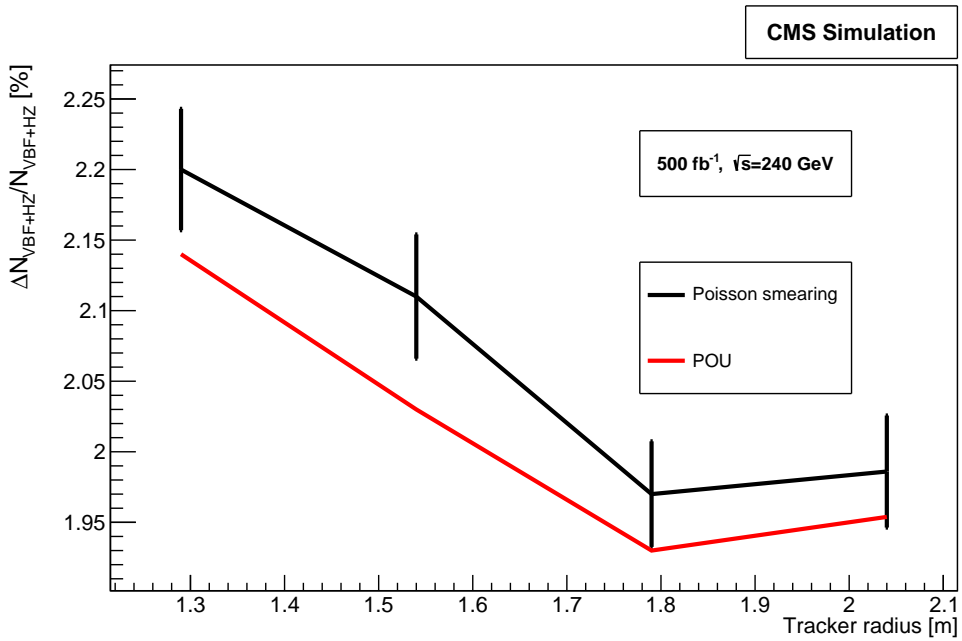


Figure 4.6: Precision of  $\Delta N_{HZ+VBF}/N_{HZ+VBF}$  while changing the tracker radius of the CMS detector.

the measurement at  $\Omega = 0.5$ . This is due to the shift in the missing mass distribution explained in 4.1.

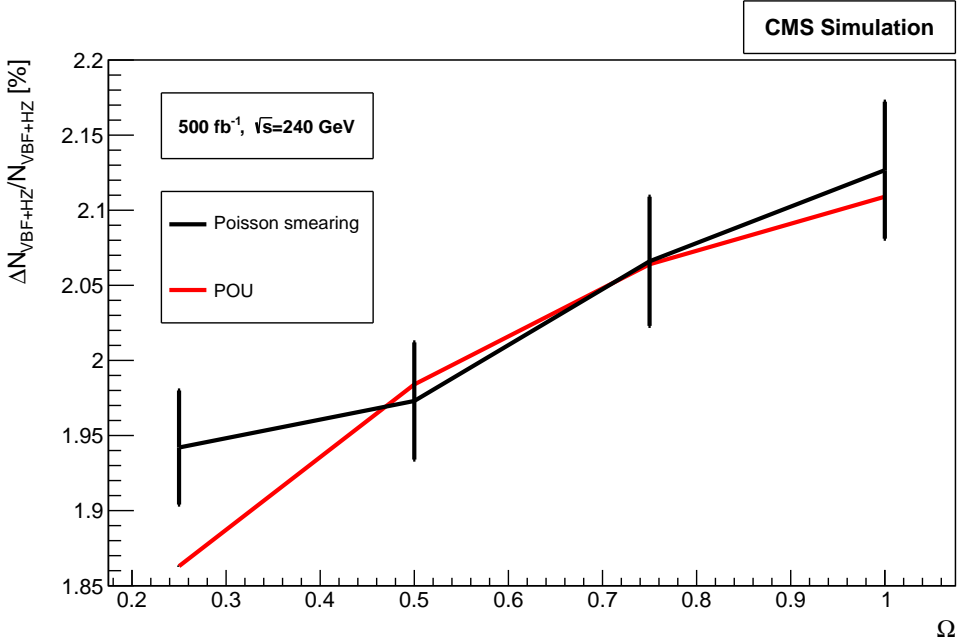


Figure 4.7: Effect of the energy resolution of the hadronic calorimeter on the precision of the  $\Delta N_{HZ+VBF}/N_{HZ+VBF}$  measurement.  $\Omega$  is the factor by which the relevant terms are changed. Only signal and ZZ background are simulated for this plot.

### 4.3 Conclusion

This analysis shows that the precision of  $\Delta N_{HZ+VBF}/N_{HZ+VBF}$  at 240 GeV and  $\Delta N_{VBF}/N_{VBF}$  at 350 GeV can be improved by tuning various detector parameters. The ILD simulation used shows an increase of precision of  $\approx 40\%$  compared to the detector variation  $\widehat{CMS}$ . Increasing the radius of the tracker inside the CMS detector by  $\approx 40\%$  increases the precision of  $\Delta N_{HZ+VBF}/N_{HZ+VBF}$  by  $\approx 10\%$  at 240 GeV. So the tracker radius, the tracker efficiency and the energy resolution of the hadronic calorimeter are identified as parameters which have a high impact on the precision of the Higgs boson cross sections measurements in the missing energy channel. The detector parameters investigated can not be indefinitely improved. However, the presented results can point the development of future detectors to the most promising direction. To improve this study one can optimize the event selection for each detector variation because the distributions are shifted if the energy resolution increases. This could further increase the improvement of the studied detector designs. Furthermore, the effect of other important detector parameters like the magnetic field or the cluster size of the electromagnetic calorimeter could be examined. Moreover, it should be noted that this study only studied the precision obtained from the missing energy channel. The precision obtained in other channels like the four-jet or the leptonic channel may depend on different detector parameters.

# Appendix A

## PYTHIA sample main program

```
! main03.cmnd.
! This file contains commands to be read in for a Pythia8 run.
! Lines not beginning with a letter or digit are comments.
! Names are case-insensitive - but spellings-sensitive!
! The settings here are illustrative, not always physics-motivated.

! 1) Settings used in the main program.

Main:numberOfEvents = 1000           ! number of events to generate
Main:timesAllowErrors = 3            ! how many aborts before run stops

! 2) Settings related to output in init(), next() and stat().

Init:showChangedSettings = on       ! list changed settings
Init:showChangedParticleData = off ! list changed particle data
Next:numberCount = 100              ! print message every n events
Next:numberShowInfo = 1              ! print event information n times
Next:numberShowProcess = 1           ! print process record n times
Next:numberShowEvent = 0             ! print event record n times

Random:setSeed = on
Random:seed = 12345
```

```
! 3) Beam parameter settings. Values below agree with default ones.  
Beams:idA = 11                                ! first beam, p = 2212, pbar = -2212  
Beams:idB = -11                                ! second beam, p = 2212, pbar = -2212  
  
! 4) Hard process : ZH at 240 GeV  
  
Beams:eCM = 240.                                ! CM energy of collision  
  
HiggsSM:ffbar2HZ = on  
23:onMode = on  
25:onMode = on
```

# Appendix B

## CMS.py

```
from detector import Detector, DetectorElement
import material as material
from geometry import VolumeCylinder
import math
import heppy.statistics.rrandom as random

class ECAL(DetectorElement):

    def __init__(self):
        volume = VolumeCylinder('ecal', 1.55, 2.1, 1.30, 2. )
        mat = material.Material('ECAL', 8.9e-3, 0.275)
        self.eta_crack = 1.479

        self.emin = {'barrel':0.3, 'endcap':1.}
        self.eres = {'barrel':[4.22163e-02, 1.55903e-01, 7.14166e-03],
        'endcap':[-2.08048e-01, 3.25097e-01, 7.34244e-03] }
        self.eresp = {'barrel':[1.00071, -9.04973, -2.48554],
        'endcap':[9.95665e-01, -3.31774, -2.11123] }
        super(ECAL, self).__init__('ecal', volume, mat)

    def energy_resolution(self, energy, eta=0.):
        part = 'barrel'
        if abs(eta)>1.479 and abs(eta)<3.0:
```

```

        part = 'endcap'
        stoch = self.eres[part][0] / math.sqrt(energy)
        noise = self.eres[part][1] / energy
        constant = self.eres[part][2]
        return math.sqrt( stoch**2 + noise**2 + constant**2)

def energy_response(self, energy, eta=0):
    part = 'barrel'
    if abs(eta)>self.eta_crack:
        part = 'endcap'
    return self.eresp[part][0]/(1+math.exp
((energy-self.eresp[part][1])
/ self.eresp[part][2]))

def cluster_size(self, ptc):
    pdgid = abs(ptc.pdgid())
    if pdgid==22 or pdgid==11:
        return 0.04
    else:
        return 0.07

def acceptance(self, cluster):
    energy = cluster.energy
    eta = abs(cluster.position.Eta())
    if eta < self.eta_crack:
        return energy>self.emin['barrel']
    elif eta < 2.93:
        return energy>self.emin['endcap'] and cluster.pt>0.2
    else:
        return False

def space_resolution(self, ptc):
    pass

```

```

class HCAL(DetectorElement) :

    def __init__(self):
        volume = VolumeCylinder('hcal', 2.9, 3.6, 1.9, 2.6 )
        mat = material.Material('HCAL', None, 0.17)
        self.eta_crack = 1.3

        self.eres = {'barrel':[0.8062, 2.753, 0.1501],
        'endcap':[6.803e-06, 6.676, 0.1716]}
        self.eresp = {'barrel':[1.036, 4.452, -2.458],
        'endcap':[1.071, 9.471, -2.823]}
        super(HCAL, self).__init__('ecal', volume, mat)

    def energy_resolution(self, energy, eta=0.):
        part = 'barrel'
        if abs(eta)>self.eta_crack:
            part = 'endcap'
        stoch = self.eres[part][0] / math.sqrt(energy)
        noise = self.eres[part][1] / energy
        constant = self.eres[part][2]
        return math.sqrt( stoch**2 + noise**2 + constant**2)

    def energy_response(self, energy, eta=0.):
        part = 'barrel'
        if abs(eta)>self.eta_crack:
            part = 'endcap'
        return self.eresp[part][0]/(1+math.exp
        ((energy-self.eresp[part][1])
        /self.eresp[part][2])))

    def cluster_size(self, ptc):
        return 0.2

```

```

def acceptance(self, cluster):
    energy = cluster.energy
    eta = abs(cluster.position.Eta())
    if eta < self.eta_crack :
        if energy>1.:
            return random.uniform(0,1)<(1/(1+math.exp
((energy-1.93816)/(-1.75330))))
        else:
            return False
    elif eta < 3. :
        if energy>1.1:
            if energy<10.:
                return random.uniform(0,1)<(1.05634-1.66943e-01*
energy+1.05997e-02*(energy**2))
            else:
                return random.uniform(0,1)<(8.09522e-01/
(1+math.exp((energy-9.90855)/-5.30366)))
        else:
            return False
    elif eta < 5.:
        return energy>7.
    else:
        return False

def space_resolution(self, ptc):
    pass

class Tracker(DetectorElement):

    def __init__(self):
        volume = VolumeCylinder('tracker', 1.29, 1.99)

```

```

mat = material.void
super(Tracker, self).__init__('tracker', volume, mat)

def acceptance(self, track):
    pt = track.pt
    eta = abs(track.p3.Eta())

    if eta < 1.74 and pt>0.2:
        return True
    elif eta < 2.5 and pt>0.5:
        return random.uniform(0,1)<0.9
    else:
        return False

def pt_resolution(self, track):
    pt = track.pt
    return 1.1e-2

class Field(DetectorElement):

    def __init__(self, magnitude):
        self.magnitude = magnitude
        volume = VolumeCylinder('field', 2.9, 3.6)
        mat = material.void
        super(Field, self).__init__('tracker', volume, mat)

class BeamPipe(DetectorElement):

    def __init__(self):
        factor = 1.0
        volume = VolumeCylinder('beampipe',
2.5e-2*factor+0.8e-3, 1.98, 2.5e-2*factor, 1.9785 )
        mat = material.Material('BeamPipe', 35.28e-2, 0)

```

```
super(BeamPipe, self).__init__('beampipe', volume, mat)

class CMS(Detector):

    def __init__(self):
        super(CMS, self).__init__()
        self.elements['tracker'] = Tracker()
        self.elements['ecal'] = ECAL()
        self.elements['hcal'] = HCAL()
        self.elements['field'] = Field(3.8)
        self.elements['beampipe'] = BeamPipe()

cms = CMS()
```

# Bibliography

- [1] **TLEP Design Study Working Group** Collaboration, M. Bicer *et al.*, “First Look at the Physics Case of TLEP,” *JHEP* **01** (2014) 164, arXiv:1308.6176 [hep-ex].
- [2] Wikipedia, “Standard model,” 2017.  
[https://en.wikipedia.org/wiki/Standard\\_Model](https://en.wikipedia.org/wiki/Standard_Model). [Online; accessed 23-January-2017].
- [3] **CMS** Collaboration, S. Chatrchyan *et al.*, “The CMS experiment at the CERN LHC,” *JINST* **3** (2008) S08004.
- [4] “Detector and physics in zeuthen for a linear collider.”  
<https://www-zeuthen.desy.de/ILC/physics/>. [Online; accessed 24-January-2017].
- [5] H. Abramowicz *et al.*, “The International Linear Collider Technical Design Report - Volume 4: Detectors,” arXiv:1306.6329 [physics.ins-det].
- [6] P. Azzi, C. Bernet, C. Botta, P. Janot, M. Klute, P. Lenzi, L. Malgeri, and M. Zanetti, “Prospective Studies for LEP3 with the CMS Detector,” arXiv:1208.1662 [hep-ex].
- [7] **ATLAS** Collaboration, G. Aad *et al.*, “The ATLAS Experiment at the CERN Large Hadron Collider,” *JINST* **3** (2008) S08003.
- [8] O. S. Bruning, P. Collier, P. Lebrun, S. Myers, R. Ostojic, J. Poole, and P. Proudlock, “LHC Design Report Vol.1: The LHC Main Ring,”.
- [9] **ATLAS** Collaboration, G. Aad *et al.*, “Observation of a new particle in the search for the Standard Model Higgs boson with the ATLAS detector at the LHC,” *Phys. Lett. B* **716** (2012) 1–29, arXiv:1207.7214 [hep-ex].

[10] CMS Collaboration, S. Chatrchyan *et al.*, “Observation of a new boson at a mass of 125 GeV with the CMS experiment at the LHC,” *Phys. Lett.* **B716** (2012) 30–61, arXiv:1207.7235 [hep-ex].

[11] CMS Collaboration, V. Khachatryan *et al.*, “Precise determination of the mass of the Higgs boson and tests of compatibility of its couplings with the standard model predictions using proton collisions at 7 and 8 TeV,” *Eur. Phys. J.* **C75** no. 5, (2015) 212, arXiv:1412.8662 [hep-ex].

[12] CERN, “The fcc-ee design study,” 2017. <http://tlep.web.cern.ch/>. [Online; accessed 23-January-2017].

[13] B. Povh, K. Rith, C. Scholz, F. Zetsche, and W. Rodejohann, *Particles and Nuclei: An Introduction to the Physical Concepts (Graduate Texts in Physics)*. Springer, 2015.

[14] T. Sjöstrand, S. Ask, J. R. Christiansen, R. Corke, N. Desai, P. Ilten, S. Mrenna, S. Prestel, C. O. Rasmussen, and P. Z. Skands, “An Introduction to PYTHIA 8.2,” *Comput. Phys. Commun.* **191** (2015) 159–177, arXiv:1410.3012 [hep-ph].

[15] M. Cacciari, G. P. Salam, and G. Soyez, “FastJet User Manual,” *Eur. Phys. J.* **C72** (2012) 1896, arXiv:1111.6097 [hep-ph].

[16] “Pythia 8 online manual,” 2017. <http://home.thep.lu.se/~torbjorn/pythia81html/Welcome.html>. [Online; accessed 18-February-2017].

[17] FCC, “Software for future circular colliders (hh, ee, he),” 2017. <https://github.com/HEP-FCC>. [Online; accessed 23-January-2017].

[18] O. Cerri, M. de Gruttola, M. Pierini, A. Podo, and G. Rolandi, “Study the effect of beam energy spread and detector resolution on the search for Higgs boson decays to invisible particles at a future  $e^+e^-$  circular collider,” arXiv:1605.00100 [hep-ex].

[19] “delphes github,” 2017. <https://github.com/delphes/>. [Online; accessed 5-February-2017].

[20] S. D. Ellis and D. E. Soper, “Successive combination jet algorithm for hadron collisions,” *Phys. Rev.* **D48** (1993) 3160–3166, arXiv:hep-ph/9305266 [hep-ph].

- [21] “Particle properties,” 2017. <http://home.thep.lu.se/~torbjorn/pythia81html/ParticleProperties.html>. [Online; accessed 24-January-2017].
- [22] S. M. Xella Hansen, C. Damerell, D. J. Jackson, and R. Hawkings, “Flavour tagging studies for a high performance vertex detector,”. [AIP Conf. Proc. 578, 799(2001)].
- [23] N. T. Meyer, *Higgs-Bosons at TESLA: Studies on Production in W W Fusion and Total Decay Width*. PhD thesis, Hamburg U., 2000. <http://www-library.desy.de/cgi-bin/showprep.pl?desy-thesis00-031>.
- [24] R. Brun and F. Rademakers, “ROOT: An object oriented data analysis framework,” *Nucl. Instrum. Meth. A* **389** (1997) 81–86.
- [25] F. James and M. Roos, “Minuit: A System for Function Minimization and Analysis of the Parameter Errors and Correlations,” *Comput. Phys. Commun.* **10** (1975) 343–367.
- [26] J. Tellinghuisen, “Statistical Error Propagation,” *J. Phys. Chem. A* **105** (2001) 3917–3921.
- [27] M. Pohl and H. J. Schreiber, “SIMDET: Version 4: A Parametric Monte Carlo for a TESLA detector,” [arXiv:hep-ex/0206009](https://arxiv.org/abs/hep-ex/0206009) [hep-ex].

## **Appendix C**

### **Eidesstattliche Versicherung**

Hiermit bestätige ich, dass die vorliegende Arbeit von mir selbständig verfasst und ich keine anderen als die angegebenen Hilfsmittel - insbesondere keine im Quellenverzeichnis nicht benannten Internet-Quellen - benutzt habe und die Arbeit von mir vorher nicht einem anderen Prüfungsverfahren eingereicht wurde. Die eingereichte schriftliche Fassung entspricht der auf dem elektronischen Speichermedium.

Ich bin damit einverstanden, dass die Bachelorarbeit veröffentlicht wird.

Hamburg, den \_\_\_\_\_ Unterschrift: \_\_\_\_\_